Numerical relativity simulations of binary neutron stars

Marcus Thierfelder,[*] Sebastiano Bernuzzi,[†] and Bernd Brügmann[‡]

Theoretical Physics Institute, University of Jena, 07743 Jena, Germany

(Dated: January 20, 2013)

We present a new numerical relativity code designed for simulations of compact binaries involving matter. The code is an upgrade of the BAM code to include general relativistic hydrodynamics and implements state-of-the-art high-resolution-shock-capturing schemes on a hierarchy of mesh refined Cartesian grids with moving boxes. We test and validate the code in a series of standard experiments involving single neutron star spacetimes. We present test evolutions of quasi-equilibrium equal-mass irrotational binary neutron star configurations in quasi-circular orbits which describe the late inspiral to merger phases. Neutron star matter is modeled as a zero-temperature fluid; thermal effects can be included by means of a simple ideal-gas prescription. We analyze the impact that the use of different values of damping parameter in the Gamma-driver shift condition has on the dynamics of the system. The use of different reconstruction schemes and their impact in the post-merger dynamics is investigated. We compute and characterize the gravitational radiation emitted by the system. Self-convergence of the waves is tested, and we consistently estimate error-bars on the numerically generated waveforms in the inspiral phase.

I. INTRODUCTION

Binary neutron stars (BNS) are among the most promising sources of gravitational waves (GWs) for ground-based interferometers of present and future generation [1–3], and are also at the origin of the powerful electromagnetic astrophysical phenomena, in particular short-gamma-ray-bursts (SGRBs) [4, 5]. While other aspects of BNS (and neutron star, NS) physics are certainly interesting, these two topics represent to date one of the most exciting observational and theoretical challenge. On the one hand, the detection of GWs emitted during the last orbits of a merger process is expected to convey unique information about the nature of matter at supra-nuclear densities which is largely unknown, e.g. [6]. On the other hand SGRBs are ultra-relativistic outflows likely to be injected during the post-merger dynamics [7–9], but neither a self-consistent model nor a simulation are yet available to provide the conditions for the "central engine" [10, 11].

A complete theoretical modeling of the late inspiral and merger phase is possible only by means of numerical relativity (NR) simulations. While BNS simulations have a longer history, see e.g. [12–14] for recent reviews, the first NR simulation was performed in [15], some years before the first complete simulations of coalescing binary black-holes (BBHs) [16–18]. Nowadays a number of NR groups are performing BNS simulations [19–25].

Recent work investigated the evolution of irrotational, circularized, equal and unequal mass binaries without magnetic fields [19, 20, 26–28]. In these works the dynamics of the system, mainly dependent on the initial masses of the stars involved, is explored in detail with particu-

lar attention on the final product of the merger: either a hyper-massive-NS (HMNS) (which eventually collapses on dynamical timescales) or a black-hole (BH) with an accretion disk configuration resulting from a prompt collapse. The gravitational radiation emitted by the systems has been characterized.

Electromagnetic fields in NR simulations of BNS have been considered in [9, 21, 22, 29, 30]. Their impact on GWs during the inspiral has been found negligible for astrophysically motivated intensities [22, 29, 30], while they have certainly a major role in the post-merger phase for several astrophysical scenarios like SGRBs. Up to now electromagnetic fields have been considered in full general relativity (GR) simulations only within the framework of ideal general relativistic magneto-hydrodynamics (GRMHD), i.e. in the limit of infinite electrical conductivity. Some efforts towards resistive GRMHD are ongoing [31].

In all cases mentioned above the studies are based on the numerical solution of the ideal general relativistic hydrodynamics equations (GRHD), or GRMHD, coupled to some 3+1 hyperbolic formulations (BSSNOK [32–34] or GHG [35]) of GR. Most of the NR results are obtained with simplified treatments of the NS interior, namely ideal gas, polytropic or piecewise polytropic equations of state (EoS). In [36] (and following works) zero-temperature (cold) "realistic" EoS are also employed. Thermal effects are expected to be relevant in the post-merger phase. They are taken into account in an approximate way using hybrid EoS [36, 37], or in simulations based on approximations of GR which instead focus more on microphysical aspects (see e.g. [38–40]). The modeling of microphysics is particularly important in combination electromagnetic fields in order to model SGRBs. Transport phenomena and neutrino physics [41–43] are currently not included in full GR BNS simulations (see however the very recent work in [44]).

We also mention that mixed binaries, i.e. binary system composed of a black-hole and a neutron star, are

*Electronic address: marcus.thierfelder@uni-jena.de
†Electronic address: sebastiano.bernuzzi@uni-jena.de
‡Electronic address: bernd.bruegmann@uni-jena.de

currently under investigation with the same techniques employed for BNSs [45–52].

While some of the above mentioned aspects of BNS physics are quite well understood, the complexity of the physical and technical problem certainly requires more investigations. On the one hand there is the need of improving the microphysical modeling of the post-merger phase, on the other hand there is the necessity to investigate the initial configuration space and to improve the accuracy of the waveforms, cf. [13].

The latter point is particularly important for future GW detection, see for example [53], also in view of a starting a program of collaboration between NR and analytical relativity community [6, 54–57]. In contrast to BBH simulations, where a precise waveform analysis is routinely performed (see e.g. [58, 59]), the accuracy of NR waveform from BNS has been poorly investigated so far. Ref. [60] reports a first error analysis of BNS waveforms. The curvature (ψ_4) waveforms are found to converge at order 1.8 in the inspiral phase and at 1.2 after the merger. The waveforms are aligned to perform the convergence test [61]. An error budget regarding the grid setting is also presented. In [57] a similar error budget regarding finite extraction, thermal and resolution effects is presented. An estimate of the phase and amplitude errors during inspiral is given based on a convergence rate assumed from other simulations [60]. The main source of error has been found to be the finite resolution. We are not aware of other detailed investigations regarding convergence and precise error estimates on the numerically generated GWs.

In this paper we present a new code to simulate non-vacuum spacetimes in full GR. The code is an extension of the BAM code developed at Jena and elsewhere [62–64] for numerical studies of multiple black holes spacetimes with adaptive mesh refinement techniques. The BAM code has been upgraded in order to solve the flux-conservative Eulerian formulation of ideal GRHD equations [65] coupled to the Einstein system. We describe in detail the equations and the implementation of HRSC scheme in BAM. The code allows the use of hybrid EoS composed of a cold part, generically provided by tables, and a thermal part modeled with an ideal gas EoS [36, 37]. A simple thermodynamical consistent procedure for table interpolation is employed.

We validate the code against a number of stringent tests involving single-star spacetimes. Each test permits the verification of a part of the numerical algorithm. Convergence and constraint violation in particular are discussed in some detail considering different reconstruction methods.

We present our first results concerning the simulation of gravitational radiation emitted from BNS evolutions. Since we do not simulate magnetic fields, our main interest is related to the GWs emitted during the inspiral phase. We focus, as a test case, on a binary already considered in the literature [22, 27, 66]. The initial irrotational configuration in quasi-circular orbit has been evolved for about three orbits, the merger and the post-merger phase with both a cold and a hot EoS. We investigate the effect of the use of different reconstruction methods on the dynamics. We report new results concerning the role of the damping parameter, η, in the Gamma-driver shift condition with regard to the dynamics. Waveforms are extracted from the simulation via a standard algorithm based on the Newman-Penrose scalar ψ_4. The actual GWs (metric waveforms) are additionally reconstructed with two different methods, namely a time-domain [67, 68] and a spectral [69] integration. The two methods are compared. We discuss the convergence of the numerically extracted GWs. Using different convergence series we provide the first consistent estimate of the errors on phase and amplitude in BNS simulations. This work is our first contribution to the study of BNS spacetime by NR simulations; the method presented here will serve as a future reference.

The structure of the paper is as follows. In Sec. II we review the basic equations solved in BAM. In Sec. III we review the description of the NS matter within BNS simulations in NR. In Sec. IV we summarize the numerical method adopted for solving the GRHD equations as well as the singularity and vacuum treatment in BAM. In Sec. V we present our results concerning single star spacetimes. In Sec. VI we present our results on simulations of BNSs.

Dimensionless units $c = G = M_\odot = 1$ are employed. Times and lengths are often expressed in ms and km to facilitate comparison with the literature. Indexes $a, b, c, ...$ run from 0 to 3, indexes $i, j, k, ...$ from 1 to 3.

II. EQUATIONS

In this section we review the equations solved in BAM. We assume the usual 3+1 decomposition of spacetime; the metric reads

$$ds^2 = -(\alpha^2 - \beta^i \beta_i)dt^2 + 2\beta_i dx^i dt + \gamma_{ij} dx^i x^j , \quad (1)$$

where α and β^i are the lapse and shift vector and γ_{ij} the spatial 3-metric. The Einstein equations are formulated in the strongly hyperbolic BSSNOK form and presented in Sec. II A. While the BSSNOK system is described in several textbooks we describe it again in the following for completeness. The equation are explicitly written for the χ-BSSNOK system not given in [62]; we point out some relevant detail for the implementation and correct some minor typos. GRHD equations are given in Sec. II B following the flux-conservative formulation of [65].

A. Metric

The BSSNOK formalism assumes the conformal decomposition of the 3-metric,

$$\tilde{\gamma}_{ij} = e^{-4\phi} \gamma_{ij} \quad \text{and} \quad \phi = \frac{1}{12} \ln \det \gamma_{ij} , \quad (2)$$

where $\tilde{\gamma}_{ij}$ is the conformal 3-metric and ϕ the conformal factor. Following [18] we introduce the variable

$$\chi \equiv e^{-4\phi} . \tag{3}$$

The extrinsic curvature K_{ij} of the spatial hypersurfaces is decomposed as

$$\tilde{A}_{ij} = \chi \left(K_{ij} - \frac{1}{3}\gamma_{ij}K \right) \quad \text{and} \quad K \equiv \gamma^{ij}K_{ij} . \tag{4}$$

The evolution system reads

$$(\partial_t - \mathcal{L}_\beta)\chi = \frac{2}{3}\alpha\chi K , \tag{5}$$

$$(\partial_t - \mathcal{L}_\beta)\tilde{\gamma}_{ij} = -2\alpha\tilde{A}_{ij} , \tag{6}$$

$$(\partial_t - \mathcal{L}_\beta)\tilde{A}_{ij} = \chi \left[-D_iD_j\alpha + \alpha(R_{ij} - 8\pi S_{ij\ \text{ADM}}) \right]^{\text{TF}} - \frac{1}{3}\tilde{\gamma}_{ij}\alpha(16\pi\rho_{\text{ADM}}) + \alpha \left(K\tilde{A}_{ij} - 2\tilde{A}_{ik}\tilde{A}^k_j \right) , \tag{7}$$

$$(\partial_t - \mathcal{L}_\beta)K = -D^iD_i\alpha + \alpha \left(\tilde{A}_{ij}\tilde{A}^{ij} + \frac{1}{3}K^2 \right) + 4\pi\alpha(\rho_{\text{ADM}} + S_{\text{ADM}}) , \tag{8}$$

$$\partial_t\tilde{\Gamma}^i = \tilde{\gamma}^{ik}\partial_j\partial_k\beta^j + \frac{1}{3}\tilde{\gamma}^{ij}\partial_j\partial_k\beta^k + \beta^j\partial_j\tilde{\Gamma}^i - \tilde{\Gamma}^j\partial_j\beta^i + \frac{2}{3}\tilde{\Gamma}^i\partial_j\beta^j - 2\tilde{A}^{ij}\partial_j\alpha \tag{9}$$

$$+ 2\alpha \left(\tilde{\Gamma}^i_{jk}\tilde{A}^{jk} - \frac{3}{2\chi}\tilde{A}^{ij}\partial_j\chi - \frac{2}{3}\tilde{\gamma}^{ij}\partial_jK - \frac{8\pi}{\chi}S^i_{\text{ADM}} \right) .$$

Above $\mathcal{L}_\beta$ is the Lie derivative along the shift vector, D_i the covariant derivative associated with γ_{ij}, R_{ij} is the Ricci tensor, see Eq. (18)-(20) in [62], and the York-ADM quantities are defined in Sec. II B. The terms proportional to ρ_{ADM} in Eqs. (7) and (8) appear because the trace of R_{ij} is obtained by substituting the Hamiltonian constraint as usual, and in Eq. (7) we choose to use the vacuum constraint in $(R_{ij})^{\text{TF}}$ and to add the missing term separately. The variables

$$\tilde{\Gamma}^i \equiv \tilde{\gamma}^{jk}\tilde{\Gamma}^i_{jk} , \tag{10}$$

defined in term of the Christoffel symbols of the conformal metric, are promoted to new evolution variables.

The constraints are

$$G_i \equiv \tilde{\gamma}_{ij}\tilde{\Gamma}^j - \tilde{\gamma}^{jk}\partial_k\tilde{\gamma}_{ij} , \tag{11}$$

$$H \equiv R - \tilde{A}^{ij}\tilde{A}_{ij} + \frac{2}{3}K^2 - 16\pi\rho_{\text{ADM}} , \tag{12}$$

$$M^i \equiv \partial_j\tilde{A}^{ij} + \tilde{\Gamma}^i{}_{jk}\tilde{A}^{jk} - \frac{2}{3}\tilde{\gamma}^{ij}\partial_j\hat{K} - \frac{3}{2}\tilde{A}^{ij}\partial_j\log\chi . \tag{13}$$

The gauge is specified by the 1+log lapse and Gamma-driver-shift [70–73]:

$$\partial_t\alpha = \beta^i\partial_j\alpha_i - \alpha^2\mu_LK , \tag{14}$$

$$\partial_t\beta^i = \mu_S\tilde{\Gamma}^i - \eta\beta^i + \beta^j\partial_j\beta^i . \tag{15}$$

The parameters are fixed to $\mu_S = 3/4$ and $\eta = 0.3$ if not stated otherwise.

B. Matter

We assume matter composed of a single particle species (simple fluid) and described by the perfect fluid stress-energy tensor

$$T_{ab} = \rho h u_a u_b + p g_{ab} , \tag{16}$$

where ρ is the rest-mass density, ϵ is the specific internal energy, $h \equiv 1 + \epsilon + p/\rho$ is the specific enthalpy, p is the pressure, and u^a is the 4-velocity ($u^a u_a = -1$) of the fluid. The total energy density is given by $e = \rho(1 + \epsilon)$.

The GRHD equations for the perfect fluid matter (ideal GRHD) are the local conservation law for the energy-momentum tensor, the conservation law for the baryon number, and the equation of state of the fluid:

$$\nabla_a T^{ab} = 0 , \tag{17}$$

$$\nabla_a (\rho u^a) = 0 , \tag{18}$$

$$P(\rho, \epsilon) = p . \tag{19}$$

Following [65] we rewrite Eqs. (17)-(18) in first-order flux-conservative form,

$$\partial_t\vec{q} + \partial_i\vec{f}^{(i)}(\vec{q}) = \vec{s}(\vec{q}) , \tag{20}$$

by introducing the *conservative* variables

$$\vec{q} = \sqrt{\gamma}\{ D, S_k, \tau \} , \tag{21}$$

where

$$D \equiv W\rho \, ,$$
$$S_k \equiv W^2 \rho h v_k \, ,$$
$$\tau \equiv \left(W^2 \rho h - p\right) - D \, . \tag{22}$$

The simple physical interpretation of these variables is that they represent the rest-mass density (D), the momentum density (S_k) and an internal energy ($\tau = \rho_{\mathrm{ADM}} - D$) as viewed by Eulerian observers. Above v^i is the fluid velocity measured by the Eulerian observer with

$$v^i = \frac{u^i}{W} + \frac{\beta^i}{\alpha} = \frac{1}{\alpha}\left(\frac{u^i}{u^0} + \beta^i\right) \, . \tag{23}$$

W is the Lorentz factor between the fluid frame and the Eulerian observer, $W = 1/\sqrt{1 - v^2}$, with $v^2 = \gamma_{ij} v^i v^j$. The fluxes in Eq. (20) are

$$\vec{f}^{(i)} = \sqrt{-g}\left\{ D\left(v^i - \frac{\beta^i}{\alpha}\right) \, , S_k\left(v^i - \frac{\beta^i}{\alpha}\right) + p\delta_k^i \, , \tau\left(v^i - \frac{\beta^i}{\alpha}\right) + pv^i \right\} \, , \tag{24}$$

while the source terms are

$$\vec{s} = \sqrt{-g}\left\{ 0, T^{ab}\left(\partial_a g_{ak} - \Gamma_{ab}^\delta g_{\delta k}\right), \alpha\left(T^{a0}\partial_a \ln\alpha - T^{ab}\Gamma_{ab}^0\right)\right\} \tag{25}$$

$$= \sqrt{-g}\left\{ 0, T^{00}\left(\frac{1}{2}\beta^i\beta^j\partial_k\gamma_{ij} - \alpha\partial_k\alpha\right) + T^{0i}\beta^j\partial_k\gamma_{ij} + T_i^0\partial_k\beta^i + \frac{1}{2}T^{ij}\partial_k\gamma_{ij}, \right.$$
$$\left. T^{00}\left(\beta^i\beta^j K_{ij} - \beta^i\partial_i\alpha\right) + T^{0i}\left(2\beta^j K_{ij} - \partial_i\alpha\right) + T^{ij}K_{ij}\right\} \, . \tag{26}$$

Above $g \equiv \det g_{ab} = -\alpha^2\gamma$ with $\gamma \equiv \det\gamma_{ij}$. From straightforward calculations the stress-energy tensor is

$$T^{00} = \frac{\rho h W^2 - p}{\alpha^2} \, , \tag{27}$$

$$T^{0i} = \frac{\rho h W^2(v^i - \frac{\beta^i}{\alpha})}{\alpha} + \frac{p\beta^i}{\alpha^2} \, , \tag{28}$$

$$T^{ij} = \rho h W^2(v^i - \frac{\beta^i}{\alpha})(v^j - \frac{\beta^j}{\alpha}) + p(\gamma^{ij} - \frac{\beta^i\beta^j}{\alpha^2}) \tag{29}$$

$$T_i^0 = \frac{\rho h W^2}{\alpha}v_i \, . \tag{30}$$

Note that both the fluxes and the source terms depend also on the *primitive* variables $\vec{w} = \{p, \rho, \epsilon, v^i\}$, and the source terms do not depend on derivatives of T_{ab}. Eq. (20) above conserves exactly the rest-mass (or baryonic mass),

$$M_0 \equiv \int d^3x \, q^0 = \int d^3x \, \sqrt{\gamma}D \, . \tag{31}$$

Standard York-ADM matter variables are easily recovered

$$\rho_{\mathrm{ADM}} \equiv n^a n^b T_{ab} = \rho h W^2 - p = \tau + D \, , \tag{32}$$

$$S_{\mathrm{ADM}}^i \equiv -n^a\gamma^{ib}T_{ab} = \rho h W^2 v^i = S^i \, , \tag{33}$$

$$S_{\mathrm{ADM}}^{ij} \equiv \gamma^{ia}\gamma^{jb}T_{ab} = \rho h W^2 v^i v^j + \gamma^{ij}p \, . \tag{34}$$

The system in Eq. (20) is strongly hyperbolic provided that the EoS is causal (the sound speed is less than the speed of light) [65]. Eigenvalues (in direction x) are given by

$$\lambda_0 = \alpha v^x - \beta^x \, , \tag{35}$$

$$\lambda_\pm = \frac{\alpha}{1 - v^2 c_s^2}\left[v^x\left(1 - c_s^2\right) \pm \right. \tag{36}$$
$$\left. c_s\sqrt{(1 - v^2)[\gamma^{xx}(1 - v^2 c_s^2) - v^x v^x(1 - c_s^2)]}\right] - \beta^x \, .$$

The others are obtained by permutation of indexes. Above the sound speed is defined by

$$c_s^2 = \left(\chi + \frac{P}{\rho^2}\kappa\right)\frac{1}{h} \, , \tag{37}$$

$$\chi \equiv \frac{\partial P}{\partial \rho} \quad , \quad \kappa \equiv \frac{\partial P}{\partial \epsilon} \, . \tag{38}$$

Note the notation conflict between χ and the metric variable defined in Sec. II A, which is resolved in the following by the context of the discussion. In the Sec. III we discuss the modeling of NS interior, i.e. the EoS of the fluid.

III. DESCRIPTION OF NS MATTER

The exact nature of the internal structure of a NS is unknown. The standard picture assumes that the matter of an isolated NS in hydrostatic equilibrium is strongly degenerate and at thermodynamic equilibrium. Consequently temperature effects are neglected and the matter is in its ground state: cold catalyzed matter. Under these conditions the EoS has one-parameter character [74], $p = P(\rho)$. Note that if one has an one-parameter

EoS the GRHD equation for τ is equivalent to that for D and thus redundant. A simple cold EoS often employed in NR simulations is the polytropic EoS

$$P(\rho) = K\rho^{\Gamma} , \qquad (39)$$

where K and Γ are parameters. The polytropic EoS describes isentropic fluids and it is equivalent to the well known ideal gas

$$P(\rho, \epsilon) = (\Gamma - 1)\rho\epsilon , \qquad (40)$$

if the flow remains smooth, i.e. no shock-heating. The parameter for a relativistic Fermi gas is $\Gamma = 4/3$, and $1 < \Gamma < 3$ for NS simulations. Note that it coincides with the adiabatic index of the fluid,

$$\Gamma \equiv c_s^2 \left(\frac{e}{P} + 1 \right) . \qquad (41)$$

The constant K in Eq. (39) fixes the entropy. Ideal gas and polytropic EoSs provide a simple and analytical description of NS matter, even though it is quite rough and approximate.

The NS structure consists qualitatively [75] of an outer region (outer crust) that extends until the neutron drip $e_{drip} \sim 10^{11}$ g cm^{-3}, an inner crust up to nuclear densities, $e_{nuc} \gtrsim 10^{14}$ g cm^{-3}, which characterize the central core. The composition of the inner and outer crust is reasonably well understood. Matter in the outer crust consists of a Coulomb lattice immersed in an electron gas; the pressure is dominated by electron pressure. As density increases, the pressure contribution from neutrons becomes larger, and in the inner crust the EoS softens due to the attractive long-range behavior of the strong interaction. Models for the outer and inner crust are for example the BPS [76] and the BBP [77], or HP94 [78] EoSs, respectively. At densities $e > e_{nuc}$ nuclei are not stable and a plasma of nucleons dominates the pressure. The EoS stiffens due to the repulsive short-range character of strong interactions. The modeling of the matter in the core is difficult and requires assumptions on the nucleon-nucleon potential and the solution of the many-body problem. Further complications are the presence of hyperons and the necessity to solve the relativistic many-body problem, super-fluidity, pion condensation, and phase transition to quark matter.

The NS core contains most of the mass (98%), while only a very small fraction is in the outer crust (10^{-5} %). Despite this the (outer and inner) crust plays the major role in defining tidal the deformation-disruption (mass-shedding limit) during evolutionary scenarios. Several EoS for the core are proposed in the literature, see e.g. [79, 80]. We refer to the set of these EoSs generically as *realistic* EoS. They are provided by tables, or, alternatively, they can be phenomenologically parametrized by piecewise polytropes [81]. Most of the realistic EoSs are considered "equivalent" since they are able to produce NSs with mass and radii that agree with observational constraints. See e.g. [82–84] and references therein for a detailed report on observational constraints on NS EoSs. Gravitational waves emission from pulsating NSs represents a unique opportunity to constrain the EoS of the core [85].

In a dynamical scenario (e.g. merger or collapse) NS matter can be heated, thus acquiring a thermal component. This situation can not be modeled if cold (one-parameter) EoS are employed and the use of a *hot* (temperature dependent) EoS is necessary. The simplest hot EoS is the ideal gas Eq. (40). A simple way to extend nuclear cold EoS to include a hot component is presented in [36]. Given values of ρ and ϵ, a hot part is allowed evolving also the τ equation and defining a "hot internal energy" as the difference between the actual ϵ and the ϵ^{cold} from the realistic cold EoS,

$$\epsilon^{hot} \equiv \epsilon - \epsilon^{cold} . \qquad (42)$$

The pressure is augmented with a thermal component which is modeled via a simple ideal gas EoS,

$$P(\rho, \epsilon) = P^{cold}(\rho) + P^{hot}(\rho, \epsilon) \qquad (43)$$
$$= P^{cold}(\rho) + (\Gamma - 1)\rho\epsilon^{hot} . \qquad (44)$$

The following relations hold:

$$\chi = \frac{2P^{cold}}{\rho} + \rho^2 \frac{d^2\epsilon^{cold}}{d\rho^2} \qquad (45)$$
$$+ (\Gamma - 1)\epsilon^{hot} - (\Gamma - 1)\rho \frac{d\epsilon^{cold}}{d\rho} ,$$
$$\kappa = (\Gamma - 1)\rho . \qquad (46)$$

Note that the adiabatic index in this case does not coincides with the sum of the "cold" adiabatic index and the ideal gas Γ. Hot EoSs constructed in this way are called *hybrid*. A study of the validity of this approach can be found in [37]. Note that obviously the hybridization of the polytropic EoS is the ideal gas EoS.

The only complete (including temperature dependence) microphysical EoSs have been developed by Shen et al. [86], Lattimer and Swesty [87], and recently by Shen G. et al [88, 89]. They allow inclusion of neutrino emission schemes, e.g. [90], and currently provide the best model to describe high density NS matter.

In addition to the analytic ones, our code can handle cold EoSs provided by tables and implements the hybridization procedure described above. While the code is ready to host hot complete EoS, we do not consider them in this work and postpone their use to the future.

IV. NUMERICAL METHOD

Our code is part of the BAM code [62–64], extending it with a module for GRHD. In the following we focus only on the matter solver, referring to [62] for a description of the code infrastructure and the algorithm for the solution of the Einstein equations via the BSSNOK scheme. We

mention only that the evolution algorithm is based on the method of lines (MoL) with explicit Runge-Kutta methods (3rd order in this work) and finite differences in space (4th order in this work). Mesh refinement is provided by a hierarchy of cell-centered nested Cartesian grids and Berger-Oliger time stepping. Metric variables are interpolated in space by means of 4th order Lagrangian polynomials and matter conservatives by a 4th order WENO scheme (see below for details about the latter). Interpolation in Berger-Oliger time stepping is performed at 2nd order. Some of the mesh refinement levels can be dynamically moved and adapted during the time evolution according to the technique of "moving boxes". GWs are extracted using the ψ_4 formalism (see Sec. III of [62]).

The algorithm implemented for the matter is a robust high-resolution-shock-capturing (HRSC) method [91, 92] based on a central scheme for the numerical fluxes. It has been successfully used and tested in spherical symmetry in [93]. HRSC schemes represent nowadays the state-of-the-art methods to solve GRHD equations since they can properly handle physical shocks, steep gradients and high Lorentz factors in relativistic plasma. In the following we describe in detail our implementation as well as the implementation of the EoS interface and the treatment of vacuum regions and spacetime singularities.

A. HRSC scheme for matter

The GRHD equations are solved by means of a HRSC method [91, 92] which considers the semi-discrete form of the equations and combines the Runge-Kutta integration with a cell-centered scheme for the RHS based on robust central schemes or simple Riemann solvers [94]. Both the time stepping and the spatial refined mesh are shared with the metric system. Our implementation follows quite closely the algorithm presented in [95] (see also [94, 96–99]). The semi-discrete form of Eq. (20) is

$$\frac{d\vec{q}_{i,j,k}}{dt} = \vec{s}_i + \frac{1}{h}\left(\vec{F}_{i-\frac{1}{2},j,k} - \vec{F}_{i+\frac{1}{2},j,k}\right) + \text{other directions} ,$$
(47)

where h is the grid spacing and $\vec{F}_{i\pm\frac{1}{2},j,k}$ are the numerical fluxes (both in the x direction). For simplicity the description is limited to 1D since all the steps necessary to construct the numerical fluxes can be (and actually are) performed in one direction at a time. In Eq. (47) the difference of the numerical fluxes is the Taylor approximation, at a certain order r, for the divergence of the fluxes

$$h\vec{f}'(x_i) = \left(\vec{F}_{i+\frac{1}{2}} - \vec{F}_{i-\frac{1}{2}}\right) + \mathcal{O}(h^r) ,$$
(48)

$$\vec{F}_{i+\frac{1}{2}} \equiv \vec{f}_{i+\frac{1}{2}} + \sum_{j=1}^{(r-1)/2} c_{2j}D^{(2j)}\vec{f}_{i+\frac{1}{2}} ,$$
(49)

where the interface fluxes $\vec{f}_{i+\frac{1}{2}}$ are computed with a Riemann solver and the $D^{(2j)}$ is a discrete operator

which approximates derivatives of order $2j$. We consider only 2nd order schemes, which amounts to dropping high-order terms in Eq. (49). The interface fluxes are computed by the local Lax-Friedrichs (LLF) central scheme [94, 97], or the well known two-speed HLL [100] Riemann solver. In this work we focus on LLF which, in spite of its simplicity, has been proved to be robust and competitive with respect to approximate Riemann solvers [101] also in the case of neutron star simulations [102]. The LLF flux reads

$$\vec{f}_{i+\frac{1}{2}}^{(\text{LLF})} = \frac{1}{2}\left[\vec{f}^L + \vec{f}^R - a\left(\vec{q}^L - \vec{q}^R\right)\right] .$$
(50)

The parameter a is the maximum of the local characteristic speeds (eigenvalues computed at interfaces $i \pm \frac{1}{2}$) of the system and it is the only characteristic information used. The quantities written with superscript L/R are the physical fluxes (Eq. (24)) and the conservative variables computed ("reconstructed") at the interface $i + \frac{1}{2}$. The reconstruction is performed using a non-oscillatory interpolation centered, respectively, on i (L, left) and on $i+1$ (R, right). The reconstruction step is performed on the primitive variables. Several methods are implemented in the code: linear Total Variation Diminishing (TVD) interpolation based on "minmod" (MM2) and "monotonized centered" (MC2) slope limiters (see e.g. [103] and [104]), the interpolation of the piecewise parabolic method (PPM) [105–107], and the third order convex-essentially-non-oscillatory (CENO3) algorithm by [108, 109]. The construction of the numerical fluxes requires an interpolation of metric quantities at the interfaces. We implemented both 2nd order (simple averages) and 4th order Lagrangian interpolation. The latter is the default used in all the tests presented here.

The algorithm used to recover the primitive variables depends on the choice of the EoS. In case of a general EoS we adopt the standard algorithm described in [92], that employs the EoS of the form Eq. (19) and a Newton-Raphson method. In case of cold one-parameter EoS a similar procedure is adopted but based on the equation which defines the variable D [110]. The exact equations employed as well as the methods are detailed in Appendix A.

Boundary conditions are applied on the primitive variables before the reconstruction step by simple extrapolation ("outflow").

We describe now the spatial interpolation used for the conservative variables in the mesh refinement, i.e. between levels. A non-oscillatory interpolation is necessary in order to avoid the Gibbs phenomenon. Different methods are adopted in different codes, see e.g. [111, 112]. As anticipated at the beginning of the section we adopt a 4th order WENO algorithm as described in [113]. The 1D scheme is summarized in the following. Given the four points $x_{i-1}, x_i, x_{i+1}, x_{i+2}$ and the corresponding data $f_{i-1}, f_i, f_{i+1}, f_{i+2}$, two candidate interpolating polyno-

mials are constructed as

$$
\begin{aligned}
p_1(x) &= f_i + \frac{f_{i+1} - f_{i-1}}{2h}(x - x_i) + \\
&\quad \frac{f_{i+1} - 2f_i + f_{i-1}}{2h^2}(x - x_i)^2 \ , \\
p_2(x) &= f_i + \frac{-f_{i+2} + 4f_{i+1} - 3f_i}{2h}(x - x_i) + \\
&\quad \frac{f_{i+2} - 2f_{i+1} + f_i}{2h^2}(x - x_i)^2 \ .
\end{aligned}
\tag{51}
$$

The final interpolated value is given by

$$
p(x) = w_1(x)p_1(x) + w_2(x)p_2(x) \ ,
\tag{52}
$$

where the weights are

$$
w_i = \frac{\alpha_i(x)}{\alpha_1(x) + \alpha_2(x)} \ ,
\tag{53}
$$

$$
\alpha_i = \frac{C_i(x)}{(\varepsilon + \mathrm{IS}_i)^2} \ .
\tag{54}
$$

The weights are defined in term of the smoothness indicators

$$
\begin{aligned}
\mathrm{IS}_1 &= \frac{25}{12}f_{i+1}^2 + \frac{64}{12}f_i^2 + \frac{13}{12}f_{i-1}^2 + \\
&\quad \frac{26}{12}f_{i+1}f_{i-1} - \frac{52}{12}f_i f_{i-1} - \frac{76}{12}f_{i+1}f_i \ , \\
\mathrm{IS}_2 &= \frac{25}{12}f_i^2 + \frac{64}{12}f_{i+1}^2 + \frac{13}{12}f_{i+2}^2 + \\
&\quad \frac{26}{12}f_{i+2}f_i - \frac{52}{12}f_{i+2}f_{i+1} - \frac{76}{12}f_{i+1}f_i \ ,
\end{aligned}
\tag{55}
$$

and the optimal weights

$$
C_1(x) = \frac{x_{i+2} - x}{3h} \ ,
\tag{56}
$$

$$
C_2(x) = \frac{x - x_{i-1}}{3h} \ .
\tag{57}
$$

In the case of a smooth function, the interpolation reduces to standard 4th order Lagrangian interpolation. For less regular functions the order of interpolation drops based on the local continuity of the derivatives (see discussions in e.g. [114, 115]). In the implementation we set $\varepsilon = 10^{-6}$ to avoid division by zero. The algorithm has been slightly modified in order to enforce monotonicity in the solution [20]. If $p_i(x)$ at a given point is larger or smaller than all four function values f_i, we set the corresponding α_i to zero. If all α_i are zero we use linear interpolation.

Finally we comment about the overall convergence rate expected in the simulation data. The different elements of the algorithm described above contribute differently to the error budget, some errors converge away more rapidly while others dominate. According to our previous experience with black hole spacetimes and to other results in the literature, we expect the overall error to be dominated by the truncation error of the finite difference discretization of the right-hand-side. In this case the matter

HRSC scheme is 2nd order accurate at most, thus the evolved fields and the relevant post-processed quantities, such as the gravitational waves and the constraints, are expected to converge to the continuum solution at this rate.

B. Equation of state

Polytropic and ideal gas EoSs are analytical and do not require special treatment. However the use of realistic EoSs, provided in form of tables, poses the problem of interpolation. A major requirement is that the interpolation is consistent with thermodynamics. The application of the first law at zero temperature translates into the relation

$$
P(\rho) = \rho^2 \frac{d\epsilon}{d\rho} \ .
\tag{58}
$$

Several methods are adopted in the literature. Widely used is a simple and efficient linear interpolation, see e.g. [116], which is not thermodynamically consistent. Hermite polynomials can be adopted for a thermodynamically consistent interpolation of general EoSs [117]. After [118] analytic fits of the tables were also used in simulations [36] in a thermodynamical consistent way.

In our code we adopt the following thermodynamically consistent procedure for cold EoS. In GRHD evolutions the quantities provided by the EoS are p, χ and κ. They are obtained in two steps. First, for a given ρ we construct $\epsilon(\rho)$ and its derivatives by interpolating the logarithms, i.e. the function $y(x)$ with $y = \log_{10}\epsilon$ and $x = \log_{10}\rho$. Derivatives are taken consistently from the interpolating polynomial. Second, the pressure is obtained from Eq. (58) together with χ, which requires $\epsilon''(\rho)$ (see Eq. (45)). For cold EoS $\kappa = 0$. Because of the second derivative, in order not to lose the term $\propto \epsilon''(\rho)$, a quadratic interpolation must be employed at least. We consider the cubic interpolation formulas given either by the standard Lagrangian four points (centered) stencil or by Hermite polynomials, e.g. [119]. In the latter case a table of the derivative $y'(x)$ must be provided, and it is computed consistently from Eq. (58). An important point for the accuracy of the interpolation procedure is the interpolation of the logarithms. In the tests performed here no relevant differences are found between Lagrangian and Hermite interpolations. The method fits also for the cold part of the hybrid EoS described in Sec. III.

C. Vacuum treatment

Of particular importance in the simulation of an isolated object is the treatment of the vacuum part. The GRHD equations in vacuum formally do not apply and the numerical algorithm can not be employed directly because the equations to recover the primitives from

the conservatives are singular (see expressions in Appendix A).

The problem of simulating fluid-vacuum interfaces is quite generic in fluid dynamics and typically a challenge already at the Newtonian level [103]. A correct, general and robust solution is not currently available even without the complication of dynamical spacetimes. A standard approach, largely employed in the literature, is instead to replace the vacuum with a minimal atmosphere of density of several orders of magnitudes smaller than the typical densities in the system. The main claim is that, since the atmosphere density is small, it will have a negligible dynamical impact. In case of NSs the situation is complicated by the presence of gravity and of a stiff fluid.

We implemented a simple vacuum algorithm based on a cold and static atmosphere. The main ideas come from [23, 110, 120]. It consists of the following main prescriptions: (i) the atmosphere density value, $\rho_{atm} \equiv f_{atm} \max \rho$, is chosen as a fraction, f_{atm}, of the maximum density; (ii) the atmosphere pressure and internal energy are chosen according to the cold part of the EoS of the evolved fluid; (iii) the atmosphere velocity is zero; (iv) the atmosphere is added to initial data in vacuum regions before starting the time evolution; (v) during the evolution, while recovering the primitive variables, a point is set to atmosphere if the density is below a threshold $\rho_{thr} \equiv f_{thr}\rho_{atm}$. Typical values used are $f_{atm} = 10^{-10}$ and $f_{thr} = 10^{2}$. In all our tests we found this approach sufficiently general and robust for our purposes.

D. Singularity treatment

The spacetime singularities treatment in BAM is based on the well known moving puncture method, e.g. [17, 18, 72, 121], which relies on the BSSNOK formulation of the Einstein equations and on the gauge choice presented in Sec. II A. This method has been proved particularly simple, elegant and robust and it is widely used in binary black hole simulations [17, 18, 62] as well as in matter simulations [27, 47, 122–125]. It has been shown in fact [126, 127] that singularities produced by collapsing matter are naturally handled by the puncture gauge without particular treatment beyond standard artificial dissipation for the metric variables.

As already pointed out in [127] however the gauge choice alone is not always enough to obtain stable and long term simulations of collapsing NSs. Unphysical values can be produced by the HRSC scheme due to numerical errors. They are typically localized in a neighborhood of the center of the collapse and appear after the formation of the apparent horizon. The origin of the problem is clear: when $v \to 1$ (or bigger due to numerical errors) the eigenvalues in Eq. (36) become singular and the formulas to recover the primitives, too (Appendix A). In order to prevent this our code sets the GRHD eigenvalues to zero if unphysical values are computed and the

TABLE I: Initial data used in single-star evolutions. Columns: name, EoS, gravitational (ADM) mass M, rest-mass M_0, equatorial proper radius R, angular momentum J scaled by the square of the ADM mass, central rest-mass density ρ_c. Polytropic models are computed with $\Gamma = 2$ and $K = 100$.

Name	EoS	M	M_0	R	J/M^2	ρ_c [$\times 10^{-3}$]
A0	polytropic	1.400	1.506	9.586	0	1.28
U0	polytropic	1.448	1.506	5.838	0	7.993
F0	FPS	1.400	1.566	7.367	0	1.906

numerical fluxes to zero whenever the velocity becomes larger than the speed of light. We found this prescription robust in the collapse of both a single star and of the HMNS produced in binary simulations. In [127] we tested other possibilities, in particular to set a ceiling on the Lorentz factor ($W_{ceil} = 10^{10}$) if the velocity becomes larger than the speed of light, as well as hydro-excision. In the case of single star collapse simulations they lead to comparable results, see Sec. V B.

V. NS SIMULATIONS

In this section we validate our code by considering evolutions of single NSs. Most of the tests presented here were suggested in [23, 24] and performed later by other groups. They include long term stability of equilibrium configurations [49, 110, 122, 128, 129], consistency of linear radial oscillations [68], migration of an unstable configuration to a stable one [110, 130], gravitational collapse to black-hole [125, 128, 131], and the evolution of a boosted star [23]. In the following we study the performance of different reconstruction procedures and the convergence of the code evolving stable equilibrium configurations. We test the EoS interpolation scheme proposed in Sec. IV B comparing evolutions with polytropic EoS in analytic and table form and considering an evolution of a stable spherical equilibrium model described by a realistic cold EoS. We demonstrate the ability of the implemented algorithm to handle shocks (migration test) and the formation of singularities (spherical collapse). The evolution of a boosted star permits the verification of a simple solution of Einstein equations in a fully dynamical and non-linear case and to test the moving boxes technique with the matter scheme. For this problem we additionally investigate the use of different values of the η parameter in the Gamma-driver shift condition.

The main properties of the initial data employed are listed in Tab. I. Most of them have been previously employed in such tests. Model A0 and U0 are polytropic $\Gamma = 2$ spherical configurations with the same rest mass; A0 is stable while U0 belongs to the unstable branch of the configurations space. Model F0 is a stable model computed with the FPS EoS [132, 133]. Spherical configurations are computed with a 2-domain spectral

code described in [93] which employs isotropic coordinates. The values of proper radii in physical units are $R = 14.156$ km, 8.621 km and 10.879 km, respectively, for models A0, U0 and F0.

The numerical grid set up for these simulations is, except for the migration and collapse test, such that the finest refinement level covers the whole star while the other refinement levels are used exclusively to the push boundary far away. This choice minimizes the effect of the noise due to the interpolation between boxes on the matter variables while it is computational more expensive for a given resolution. In the case of the migration and the collapse test more refinement levels are required to resolve the expanding or contracting fluid. Octant $(x > 0, y > 0, z > 0)$ symmetry is imposed. We use the 3rd order Runge-Kutta time stepping and a Courant-Friedrichs-Lewy (CFL) factor of 0.25. In some cases we tested also the use of 4th order Runge-Kutta finding the same results. All the figures in this section and in the following are shown for the maximum resolution unless explicitly stated otherwise.

A. Stable stars

Model A0 and F0 are stable equilibrium configurations, therefore their evolution is trivial. Since the continuum solution can not evolve but has to remain in the initial condition, the dynamics of the numerical solution is governed by truncation errors and by spurious effects due to the artificial atmosphere. This gives the possibility to study long term stability and convergence of the code. Different reconstruction schemes are considered. The grid is composed of three levels labeled $l = 0, .., 2$; the finest box covers entirely the star. Simulations are performed employing resolutions of $h_2 = 0.2, 0.3, 0.4, 0.5$ ($h_2 = 0.295, 0.443, 0.591, 0.738$ km) for the finest box and last about 10 ms.

Long term stability and convergence. We discuss here the simulations of model A0. It is well known, e.g. [23], that numerical errors trigger small amplitude pulsations of the star which oscillates at proper mode frequencies. The phenomenon is depicted in Fig. 1 where the evolution of the central rest mass density normalized to its initial value is shown for different reconstruction schemes. The figure demonstrates also the ability of the code to maintain the initial configuration. For instance the pulsations amplitude is less than 0.5% over 10 ms. Two frequencies dominates the pulsations: $\nu_F = 1421$ Hz and $\nu_H = 3959$ Hz. They agree within the errors estimated from the output time sampling (2%) with the fundamental radial linear mode and its first overtone as computed by perturbative methods [134, 135]. The figure highlights a secular drift in the case that MC2 reconstruction is adopted. A similar drift is observed also in simulations with PPM and CENO at lower resolutions. This secular drift is a feature related to the evolution of the geometry together with the fluid since, if we perform sim-
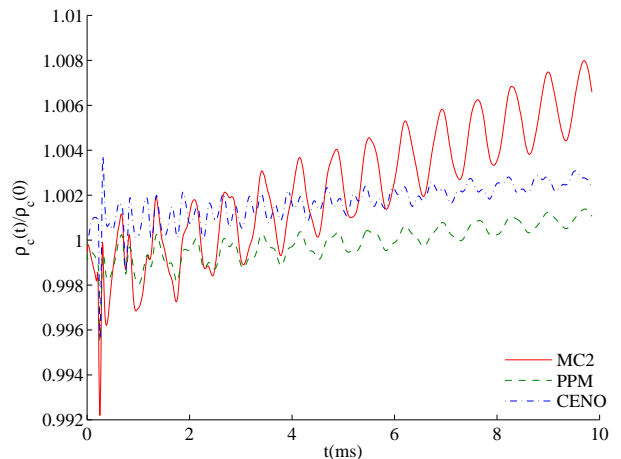

FIG. 1: Evolution of the central rest-mass density of model A0. The picture shows the normalized value $\rho_c(t)/\rho_c(0)$ for different reconstruction schemes.

ulations in the Cowling approximation (metric variables not evolved), it is almost absent at all the resolution. The amplitude of the pulsations is also larger in the case of MC2 indicating that the truncation errors are bigger as expected for a linear reconstruction. Notice that in the simulations with CENO reconstruction the overtone of the radial mode at frequency ν_H is more clearly visible.

During preliminary tests with CENO reconstruction we observed a loss of stability between 2 and 6 ms depending on the resolution employed. We found that for a compact star evolution and a standard implementation of the CENO reconstruction, the limiter tends to select in some points the lower order sub-stencils. A similar effect is also discussed in [19]. The problem is easily fixed in our set up by choosing a different weight in the weighted differences between the linear reconstruction and the quadratic polynomial with centered stencil. Specifically we set the free parameter $\alpha^0 = 0.7$ in Eq. A.6 of [109] to $\alpha^0 = 0.1$. In this way the limiter selects the central higher order stencil. We found this solution sufficient for all the problems and at all the resolutions considered in this work. We note that also the PPM reconstruction has several free parameters to tune. We did not attempt tuning but instead we use the prescription given in [136].

Next we discuss convergence. Fig. 2 reports the evolution of the L1 distance between the rest-mass density evolved and the initial data. The different curves refer to different resolutions; at every time the difference between two curves behaves as $||\rho(t) - \rho(0)||_1 \propto h^r + \mathcal{O}(h^{r+1})$ since the initial data represent also the solution for the evolution problem. The three panels from top left to bottom left refer to different reconstructions. In all the cases we observe convergence with increasing resolution; 2nd order convergence is found at early times $t \sim 2$ ms for all the methods. At late times however the MC2 and PPM reconstructions show larger truncation errors
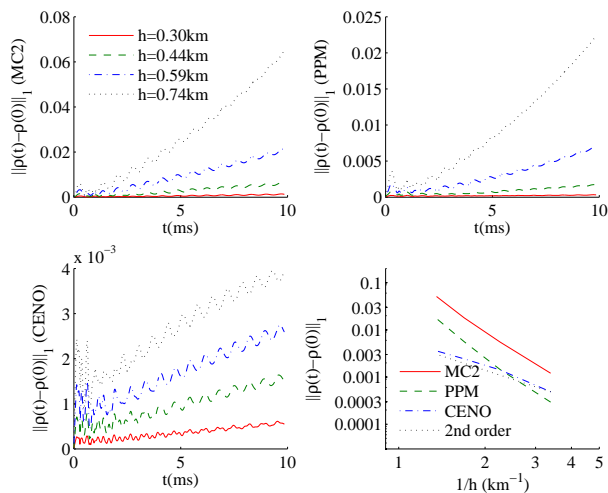
FIG. 2: Convergence in L1 norm of evolutions of model A0. The first three panels from the top-left to the bottom-right show the evolution of the L1 distance $||\rho(t)-\rho(0)||_1$. Different lines refer to different resolutions. Different panels refer to the three different reconstructions considered: MC2, PPM and CENO. The last panel (bottom-right) shows in a log-log plot the L1 distances as a function of $1/h$ at $t = 8$ ms for the three reconstructions MC2 (solid-red line), PPM (dashed-blue line) and CENO (solid-green line).

FIG. 3: Same as in Fig. 2 but results are computed in the Cowling approximation.

and the curves present a quadratic behavior. This leads to apparent over-convergent results, which indicates the simulations are not yet in the convergent regime. By contrast the use of CENO reconstruction gives 2nd order convergence over the whole simulated time. The last panel (bottom right) summarizes the observed convergence rate by showing in a log-log plot the L1 distances as a function of $1/h_2$ at $t = 8$ ms and for different reconstructions. The slope of the lines gives the convergence rate. The over-convergent behavior for MC2 and PPM as well as the 2nd order convergence of CENO are evident.

To interpret these results we recall here that in a HRSC scheme the truncation errors strongly depend on the degree of smoothness of the solution and on the specific limiter employed. While the formal convergence rate of the methods employing different reconstruction is the same (2nd order), the truncation errors for this problem are simply different in the three cases. PPM and MC2 reconstructions are only first order at smooth extrema thus they are expected to be less accurate on smooth solution than CENO, but more robust in the presence of strong shocks. More importantly the apparent over-convergence behavior is not simply related to the HRSC method employed to solve the GRHD equations, but it seems a genuine aspect of evolving the GRHD equations coupled to the Einstein equations. To show this we consider Fig. 3, which is the same as Fig. 2 but in the Cowling approximation. From an inspection of the figure it is clear that, once the metric is not evolved, all the reconstructions perform quite similarly showing perfect 2nd order convergence in
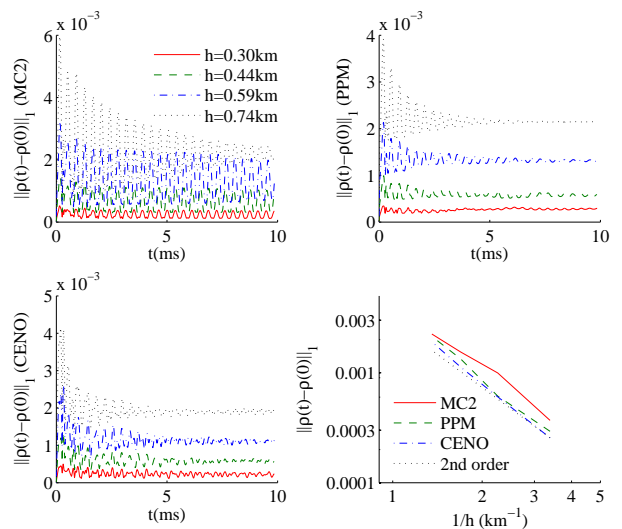
L1 norm at all times. Specifically one finds that CENO and PPM have similar performance and that for all the reconstructions the convergent regime is reached at the considered resolutions. We conclude that the slower convergence observed for MC2 and PPM in the case the metric is evolved is due to a combination of numerical errors from various part of the algorithm rather than to an effect related only to the reconstruction methods.

We finally comment on rest-mass conservation. In all the simulations reported here we observe that the deviation runs from a maximum of $\Delta M_0/M_0 \sim 10^{-2}$ with MC2 reconstruction at the lowest resolution to a minimum of $\Delta M_0/M_0 \sim 10^{-6}$ for CENO at the highest resolution. This remarkable result is a well known consequence of the use flux-conservative methods.

Constraint violation. The Einstein constraints are violated at the level of the numerical error independently of the formulation or the method adopted. When free-evolution schemes are adopted, the constraints are only monitored (not solved) and typically the violation (i) grows in time, (ii) converges with increasing resolution. In our simulations we observe this behavior. The biggest violation on the grid are found in the region covered by the matter and, at least at the initial time, at the boundary.

Fig. 4 summarizes our findings. The three panels from top-left to bottom-left show the evolution of the L2 norm of the Hamiltonian constraint for several resolutions in the cases when MC2, PPM and CENO reconstruction are employed. The violation converges to zero in all the cases. From the figures is clear that the absolute value of the violation is larger for the MC2 reconstruction while it is about a factor 10 smaller for CENO reconstruction when compared to MC2 and PPM. A summation of effects and errors as described in the previous paragraph
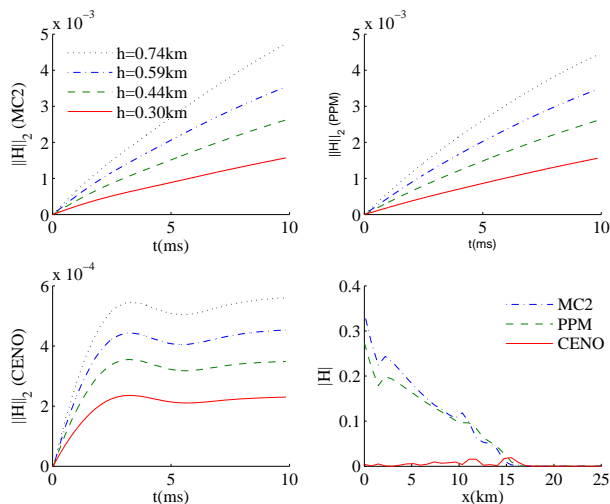
FIG. 4: Hamiltonian violation during the evolution of model A0. The first three panels from the top-left to the bottom-right show the time evolution of the 2-norm of the Hamiltonian constraint computed on the finest grid level which fully contain the star. Different lines refer to different resolutions. Different panels refer to the three different reconstructions considered: MC2, PPM and CENO. The last panel shows the profile in the x direction of the Hamiltonian constraint at time $t \sim 10$ ms for the maximum resolution and three reconstructions MC2 (solid-red line), PPM (dashed-blue line) and CENO (solid-green line). Note the different scales of the plots.

contributes to this behavior. It is difficult to clearly identify them due to the complexity of the equations and of the numerical method employed.

We observe that, if mesh refinement is not employed but only one box corresponding to the 3rd level is used, then the norm of the Hamiltonian constraint shows an anti-convergence behavior at early times. This feature is due to the initial non-convergent constraint violation at the boundary, related to the use of Sommerfeld conditions [137], which dominates the violation in the interior at early times. The use of mesh refinement is thus important to minimize the effect of the boundary conditions.

The bottom-right panel displays the spatial profile in the x direction of the Hamiltonian constraint at late time, $t \sim 10$ ms, for simulations employing the highest resolution and different reconstruction schemes. The Hamiltonian violation accumulates in time in the region of the matter. Once again the difference in the results is clear between the CENO reconstruction and PPM and MC2. In case of the unigrid simulations mentioned above the bulk violation dominates over the boundary violation after the first ms of evolution in the case that PPM or MC2 reconstruction is employed.

These tests convinced us to use the CENO reconstruction (see also Sec. VI B). We stress that if a different setting is used, e.g. a different mesh, method to solve Einstein equations, numerical flux, etc. or simply much higher resolutions, the picture may change.

The constraint accumulation and boundary condition effects discussed here are related to the use of BSSNOK and the Sommerfeld boundary condition. They have been studied in detail in [93, 137] where the Z4c formulation was proposed as an alternative. Ref. [93, 137] are restricted to spherical symmetry, but we will investigate in the future the use of Z4c in 3D.

Interpolation of EoS tables. In order to establish the performance of the interpolation scheme for EoS 1D tables described in Sec. IV B, we consider simulations of model A0 and of model F0 employing tables.

The evolutions of model A0 performed both with the analytic expression for the polytropic EoS and with a test-table do not significantly differ. As an example the central rest mass density show differences smaller than 0.01 % over 10 ms of simulated time for a resolution of $h_2 = 0.2$ ($h_2 = 0.295$ km). Performance is clearly affected by the use of tables: we observe on average a slow down of about 10 % but always less than 20%. The use of tables with different entries, e.g. 126 and 1024, does not lead to differences in these simulations.

In order to obtain an accurate evolution of model F0 we employ a table generated from the analytic fits of the FPS EoS [36, 118]. Initial tests with publicly available tables showed a progressive accumulation of round off errors as simulation time advances that eventually led to a failure during the recovery of primitives. The reason is the low accuracy of the table entries (in some cases few digits). Once tables from the fits are employed, the simulations are stable and accurate as in the polytropic case. For what concerns the proper radial frequencies of F0, we estimate $\nu_F = 3045$ Hz and $\nu_H = 7232$ Hz, with a resolution of $h_2 = 0.2$ and a total simulated time of 7 ms. They agree within few percent with perturbative results computed in [135]. As expected in this case the evolutions with the cold table and with the corresponding hybrid EoS do not differ significantly, while we observe some small differences due to the different atmosphere treatment.

B. Unstable stars

We discuss the evolution of model U0. Since it is an unstable configuration a small perturbation can cause either the migration towards a stable model of the same rest mass or the collapse to a black-hole. In practice truncation errors are enough to trigger the migration while the further addition of a small radial perturbation (bigger than the truncation errors) leads to the collapse. In the following we will consider both cases. The simulations presented here were performed with CENO reconstruction. A direct quantitative comparison of the results for the collapse with an independent 1D spherical code can be found in [127].

Migration. The dynamics of a migrating star is described in detail in [24, 130]. Within the first 0.5 ms the
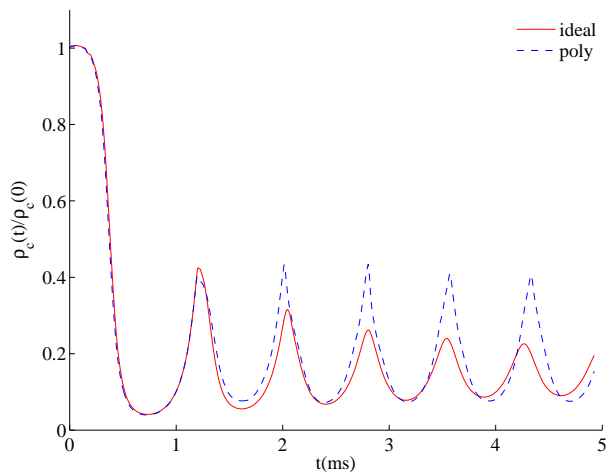
FIG. 5: Evolution of the central rest-mass density in the migration test. The picure shows the normalized value $\rho_c(t)/\rho_c(0)$ in the case of an ideal gas EoS (red solid line) and polytropic EoS (blue dashed line).
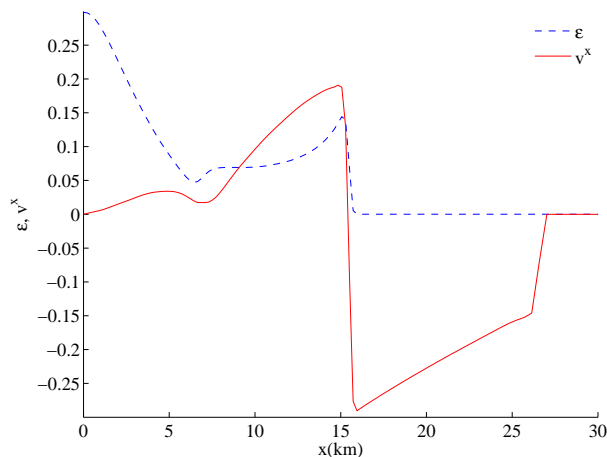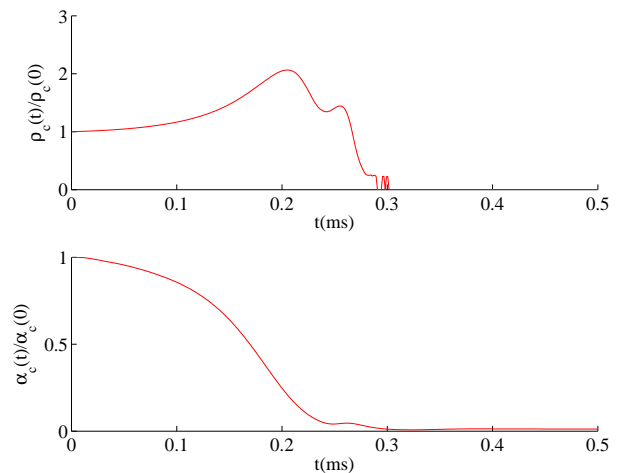

FIG. 7: Dynamics of the collapse to a black hole with puncture gauge. The picture shows the evolution of the central rest-mass density (top panel) and of the central lapse (bottom panel). Both are normalized by the central value of the initial data.

FIG. 6: Shock formation in the migration test. The picture shows the profiles of the specific internal energy ϵ and of the component v^y of the velocity at time $t \sim 1.1$ ms, i.e. soon after the shock formation. Note that only 1/10 of the numerical grid is shown.

star rapidly expands while the central density decreases by a factor 8 to $\rho_c \sim 1.4 \times 10^{-3}$; a phase of strongly nonlinear pulsations around the stable configuration then starts. The configuration reached is in fact the perturbed model A0, where the difference in the ADM mass between A0 and U0 has been converted into the kinetic energy of the pulsations. If the polytropic EoS is adopted, thus enforcing an isentropic evolution, oscillations can be damped by the effective numerical viscosity of the HRSC scheme and by spurious interaction with the atmosphere. If the ideal gas EoS is employed, thus allowing shock heating, a shock forms during the first pul-

sation at the interface between the inner core and the infalling mantle (outer lower density matter). The inner core then bounces and expands again several times feeding the shock with kinetic energy, which dissipates it into thermal energy. As a result the oscillation amplitudes decrease. Fig. 5 shows this behavior captured by our simulation; the evolution of central rest-mass density is plotted for the two different EoS. The amplitude of the pulses remains approximately constant during the simulation in the case of polytropic EoS, indicating the spurious numerical effects are negligible, while it decreases as expected in the case of the ideal gas EoS. The capture of the shock dynamics is demonstrated in Fig. 6 which shows the profile in the x direction of the specific internal energy and of the x component of the velocity at the time $t \sim 1.1$ ms, i.e. just after of the shock formation when the shock wave is moving outward. The figure clearly indicates how part of the matter is expanding outwards while the low density mantle is infalling towards the symmetry center. Note the steep profile of the velocity. We observe that, in the ideal gas EoS case, the expansion of the star extends to the boundary of the numerical grid and a fraction of the mass, 1-2 % percent over the simulated time, is lost outside [168]. The grid covers a cube of side 200 (295 km) and five levels are employed with a maximum resolution of $h_4 = 0.15$ ($h_4 = 0.221$ km) and a minimum of $h_0 = 2.4$ ($h_0 = 3.544$ km). The region within a coordinate radius of about $r \sim 50$ (74 km) is entirely resolved by the two finest refinement levels. By contrast, in the isentropic case, the expansion reaches a maximum coordinate radius of $r \sim 25$ (37 km) and the rest mass is conserved as in the stable star tests.

Collapse. The collapse is triggered by introducing a radial perturbation of the velocity field with an ampli-

tude larger than truncation errors. Since we are only interested in testing the ability of the code to handle the formation of singularities, to keep the set up simple we do not solve the constraints after imposing the perturbation. In our experience this procedure does not introduce relevant unphysical effects, while it is clearly an inconsistent way to solve Einstein equations (see also discussions in [19, 110, 138]). Furthermore the results obtained are in close qualitative agreement with [24, 130] where the constraints were solved. For these simulations we employ an eight level grid with maximum resolutions of $h_7 = 0.05, 0.03125, 0.025$ ($h_7 = 0.0738, 0.0461, 0.0369$ km) which cover a cube of side 1.164 (1.72 km).

The collapse happens in the first 0.3 ms of simulation: the matter falls towards the symmetry center while the metric varies rapidly adapting itself to the matter distribution. At about $t_{AH} \sim 0.23$ ms an apparent horizon forms with an initial coordinate radius of $r_{AH}(t_{AH}) \lesssim 0.96$ (1.41 km or 0.66 M). Part of the matter is outside of it and then rapidly accreted. Fig. 7 shows the evolution of the central rest-mass density (top panel) and that of the central lapse (bottom panel). The central density increases of a factor two at t_{AH} while the lapse collapses towards zero. After t_{AH} the gauge conditions in Eq. (14) and Eq. (15), in particular the Gamma-driver for the shift, play the main role in handling the singularity. As described in detail in [127], the shift condition deforms the spatial coordinates pushing the proper (Schwarzschild) radii $r_{Schw} \lesssim 1.7$ (2.55 km or 1.2 M) outside the innermost point of the numerical grid (see also the top panel of Fig. 6 in [127]). Consequently: (i) matter effectively disappears from the numerical grid; (ii) the end state of the collapse is the trumpet slice of Schwarzschild [72, 121, 139, 140]. The central rest-mass density in Fig. 7 reaches the atmosphere value about $\Delta t \sim 0.1$ ms after t_{AH}. Some spurious effects are visible during this time interval and they are related to the numerical treatment of the matter fields discussed in Sec. IV D. We experimented with the alternative treatments described in Sec. IV D, finding unimportant quantitative differences only in the short phase before all the matter disappears except for the atmosphere.

The behavior of the matter is also demonstrated in Fig. 8 which shows the evolution of the irreducible mass of the black hole normalized to the ADM mass of the system (solid line) and of the rest mass normalized to the initial value (dashed lines). The irreducible mass of the black hole is obviously zero at the beginning and after t_{AH} it rapidly reaches a value corresponding to the initial ADM mass of the system. The rest mass is shown computed on the finest refinement level (level 7) for the best resolution ($h_7 = 0.025$) and on a coarser one (level 5) with a resolution of $h_5/4$. Since the matter is contracting, the mass on the level 7 initially increases and after t_{AH} the level contains all the matter. Level 5 instead always contains all the matter but after t_{AH} does not resolve it properly. During the collapse the rest-mass is conserved up to 0.05% while, after t_{AH}, it rapidly decreases to the
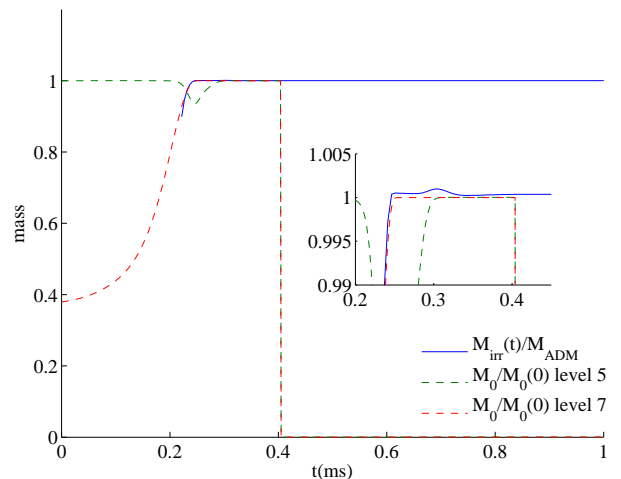

FIG. 8: Evolution of different mass quantities in the collapse test. The picture shows the irreducible mass (solid line) of the final black hole and the rest mass of the matter (dashed line) normalized to their initial values at level 5 and 7.

atmosphere value, $M_0(t > t_{AH}) \sim 10^{-6} M_0(0)$.

C. Boosted star

We discuss here the evolution of model A0 boosted in the x direction at a speed of $v = 0.5$ corresponding to a Lorentz factor of $W = 1.16$. The setup of the initial data is as described in [23]. The test is interesting because it gives the possibility to experiment in a simple scenario with several points: fully dynamical and nonlinear evolutions, the performance of the moving boxes with matter, and different gauge conditions. We use five refinement levels, the moving one is the finest which entirely covers the star. The different resolutions employed for the finest box are $h_4 = 0.4, 0.278, 0.208$ ($h_4 = 0.588, 0.408, 0.306$ km).

The solution of the evolution problem depends on the gauge conditions employed. If we choose to simply advect lapse and shift, the solution is analytic and it is just a time shift of the initial metric and matter profiles. If the conditions in Eq. (14) and Eq. (15) are used, the solution is not analytic. In order to investigate the numerical solution obtained under the 1+log and Gamma-driver condition we consider evolutions with different values of the parameter η. A similar investigation has been carried out for BNS and it is presented in Sec. VI B. Fig. 9 summarises our findings. It shows the profiles of the rest-mass density in the x direction at the final time of $t = 1.72$ ms for evolutions using different values of η. All the profiles are shifted back to the initial position of the star, the initial profile is also plotted. As apparent from the figure, the choice $\eta = 0$ corresponds to the case closest to the analytic solution, while for higher values the star
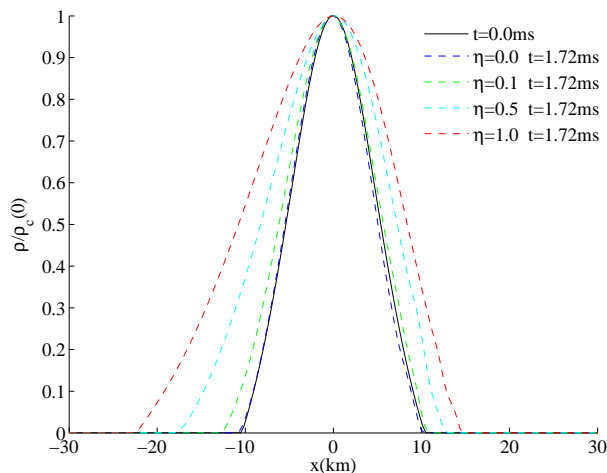
FIG. 9: Profile of rest-mass density of the evolved boosted model A0. The picture shows the rest-mass density profile normalized to the initial value at time $t = 1.72$ ms for evolutions corresponding to different values of the η parameter in the Gamma-driver shift (dashed colored lines). The profiles are shifted back to the initial position of the star, the initial data is also plotted (black solid line).
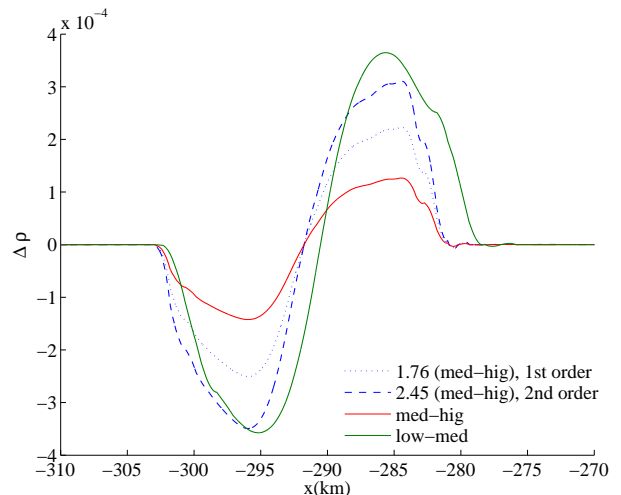

FIG. 10: Self-convergence test of the evolution of a boosted star. The pictures shows the differences between the profiles of the rest-mass density at $t = 3.95$ ms evolved with different resolutions. The labels of the solid lines "low", "med" and "hig" in the legend correspond to resolutions $h_4 = 0.4, 0.201, 0.278$. The difference between medium and high resolution is scaled for 2nd order (dashed line) and 1st order (dotted line). The gamma-driver condition employs $\eta = 0$.

profile is progressively more distorted in the direction of motion.

We finally comment about convergence. Fig. 10 shows the point-wise self-convergence the spatial profile of ρ at $t = 3.95$ ms for $\eta = 0$. We show the differences between the rest-mass density profile computed at different resolutions. The difference between the medium, $h_4 = 0.278$, and the high resolution, $h_4 = 0.208$, is scaled by a factor corresponding to 1st (dotted line) and 2nd (dashed line) order convergence. Point-wise convergence is lost at early times but the magnitude of the errors scales at about 2nd order thus indicating convergence in the L1 norm as expected. Note that the evolution time presented here is a factor of about 10^4 longer than simulations in [23].

VI. BNS SIMULATIONS

In this section we discuss our BNS simulations. We focus on a simple equal-mass irrotational configuration evolved with polytropic and ideal gas EoS. In both evolutions the formation of a HMNS is observed, but in the isentropic case it collapses after about 3 ms producing a Kerr BH surrounded by a disk of mass $M_d \lesssim 2 \times 10^{-2} M_0$, while in the other case the HMNS survives for about 9 ms before collapsing. We give an overview of the dynamics and discuss the impact of using different resolutions and different reconstructions schemes. We present results concerning the use of different values of the damping parameter η in the shift condition: while small values of η lead to less coordinate eccentricity during the inspiral, they reduce the coordinate size of the final BH. We

TABLE II: Parameters of the initial binary configuration. Columns: name, ADM mass M, rest mass M_b and ADM mass $M_\star$ of each star in isolation, angular momentum J scaled by the square of the ADM mass, gravitational wave frequency ω_0, proper separation d, central density of each star ρ_c. The parameters in the polytropic EoS are $\Gamma = 2$ and $K = 123.6489$.

name	M	M_b	$M_\star$	J/M^2	ω_0 [Hz]	d	ρ_c $[\times 10^{-4}]$
G2P14	2.998	1.625	1.499	0.4450	589	36.582	9.569

present and characterize the GWs computed from the simulations. We compute the actual GWs degree of freedom (metric waveforms) by means of the post-processing algorithms described in [67, 68] and [69] and compare their performance. Convergence tests are performed indicating 2nd order convergence of the inspiral waveforms without any time-shifting procedure. For the first time in BNS simulation, we estimated precise error-bars on the waveforms by extrapolating the results in resolution.

A. Initial data and numerical settings

We employ as initial data quasi-equilibrium configurations of irrotational equal-mass binaries in quasi-circular orbits. These initial configurations are computed with a multi-domain spectral code which solves the Einstein constraint equations under the assumption of a conformally flat metric. The code is based on the LORENE library [141] and provided by the NR group in LUTH (Meudon). These initial data represent to date the most

accurate computation of equilibrium BNSs and they are publicly available on the web. The assumption of irrotational flow is believed to be astrophysically realistic since the spin period of the neutron star is larger then the orbital period in the late inspiral. In other terms, the time of coalescence due to gravitational radiation is shorter than that of synchronization due to viscosity. Because the late inspiral and merger phases are expected to happen a very long time after the birth of the binary system ($\sim 10^8$ yr), the temperature of the matter can be assumed to be negligible. The neutron stars in the equilibrium system are thus described by the cold EoS.

The properties of the initial configuration that we consider in the following are summarized Tab. II. The binary has ADM mass $M = 2.998$, angular momentum $J = 8.836$ and proper separation $d \simeq 36.582$ (54 km), thus the compactness of the system is $M/d \simeq 0.08$. The coordinate separation is 30.457 (45 km). The rest-mass and ADM mass of each star in isolation ($d \to \infty$, spherical configuration with same rest-mass) are $M_b = 1.625$ and $M_\star = 1.499$, respectively. Note the notation for the rest-mass of the star in isolation, M_b, and for the rest-mass of the binary, M_0. The compactness of each star in isolation is $M_\star/R = 0.14$. The equilibrium configuration was first computed in [66, 142].

As a test for the implementation we performed evolutions with other initial configurations. In particular we considered an irrotational equal-mass binary described by the APR EoS [143] computed in [142, 144] and evolved in [26, 145]. The evolutions were performed using both an APR table based on the analytic fit of [145] and its hybridization with a $\Gamma = 2$ ideal gas EoS. The robustness of the procedure described in Sec. IV B has been checked also in the case of BNSs. All these tests were performed at grid configuration L, M and H0 (see below), thus we do not discuss them in the following. Another configuration whose evolution was explored is an irrotational equal-mass binary described by a polytropic EoS and with ADM mass $M = 3.251$ and compactness of each star $M_\star/R = 0.16$ [66, 142]. As expected evolutions with both polytropic and ideal gas EoSs led to a prompt collapse to a BH and the main evolution happens in 11 ms. Results are comparable to the findings in [60]. Since the evolution of model G2P14 has a more complicate post-merger dynamics we focus on the results obtained from these evolutions. They evidently represent a more stringent test for the code.

In Tab. III we report the grid configurations used for the evolution simulations. Simulations with configurations L and M can be run on a small machines. They need between 8 and 16 processors with 1GB of memory per core. While they can be carried out without any problem, thus proving the flexibility of the code, the results are too inaccurate to be considered for a sensible analysis. Convergence can be measured only in simulations employing configurations H0 as shown in the following. For each grid configuration the finest refinement level covers each star entirely. The latter is resolved with

TABLE III: Grid configurations used in BNS simulations. Columns: identifier, number of grid levels (boxes), number of moving boxes, resolution of finest box (dimensionless and km), number of points in finest box, resolution of coarsest box (dimensionless and km), number of points in coarsest box.

name	RL	MRL	h_5	h_5 [km]	N_5	h_0	h_0 [km]	N_0	boundary
L	6	4	0.500	0.74	40	16.0	23.6	80	945
M	6	4	0.400	0.59	50	12.8	18.9	100	945
H0	6	4	0.313	0.46	64	10.0	14.8	128	945
H1	6	4	0.250	0.37	80	8.0	11.8	120	709
H2	6	4	0.200	0.29	100	6.4	9.4	210	982
H3	6	4	0.156	0.23	128	5.0	7.4	260	960

128 points in runs H3 and 64 points in H0. Let us briefly comment about the grid setting used here and those used for BBH simulations, e.g. [58, 62, 146]. For BBH simulations roughly half the number of points per direction than here is used together with more grid levels (typically 9-11 levels). Higher resolutions are reached in the finest grid level in order to resolve the punctures, while comparable (or less) resolutions are used on level 5. Therefore the horizon of the final BH in BBH simulations is resolved typically on level 6 or 7 with a resolution about two to four times better than in BNS simulations. One important consequence is that the precision of the apparent horizon finder is affected.

The performance of the code for each grid configuration is reported in Tab. IV. The BNS runs described in this paper require an average speed of ~ 3 M/hr (H3) on 128 processors in the LRZ cluster (Munich) and ~ 9 M/hr (H0) on 32 processors. In physical units 10 M of the configuration selected corresponds to ~ 0.05 ms of simulation. We performed scaling tests up to 512 processors finding good scaling properties by using larger grid setups and higher resolutions. Production runs with resolutions of $h_5 \sim 0.12 - 0.10$ on 256-512 processors are thus definitely feasible in reasonable times with our code. Here we did not run such kind of simulations because of our computer time restrictions.

Our grid settings are similar to those of other codes [22, 112]. The highest resolution employed here is 30 % lower than the maximum resolution used to date on BNS simulations employing mesh-refined-Cartesian-grid-based codes [22, 56] and comparable to [26].

If not explicitly stated the data discussed refer to simulations employing RK3 time stepping, CFL factor of 0.25 and CENO reconstruction.

B. Overview of the dynamics

The initial configuration has been evolved using both the cold polytropic EoS and the ideal gas $\Gamma = 2$ EoS. In the following we will refer to the isentropic evolution with the name of the initial configuration while we will use the suffix "hot" when thermal effects are simulated. Evo-
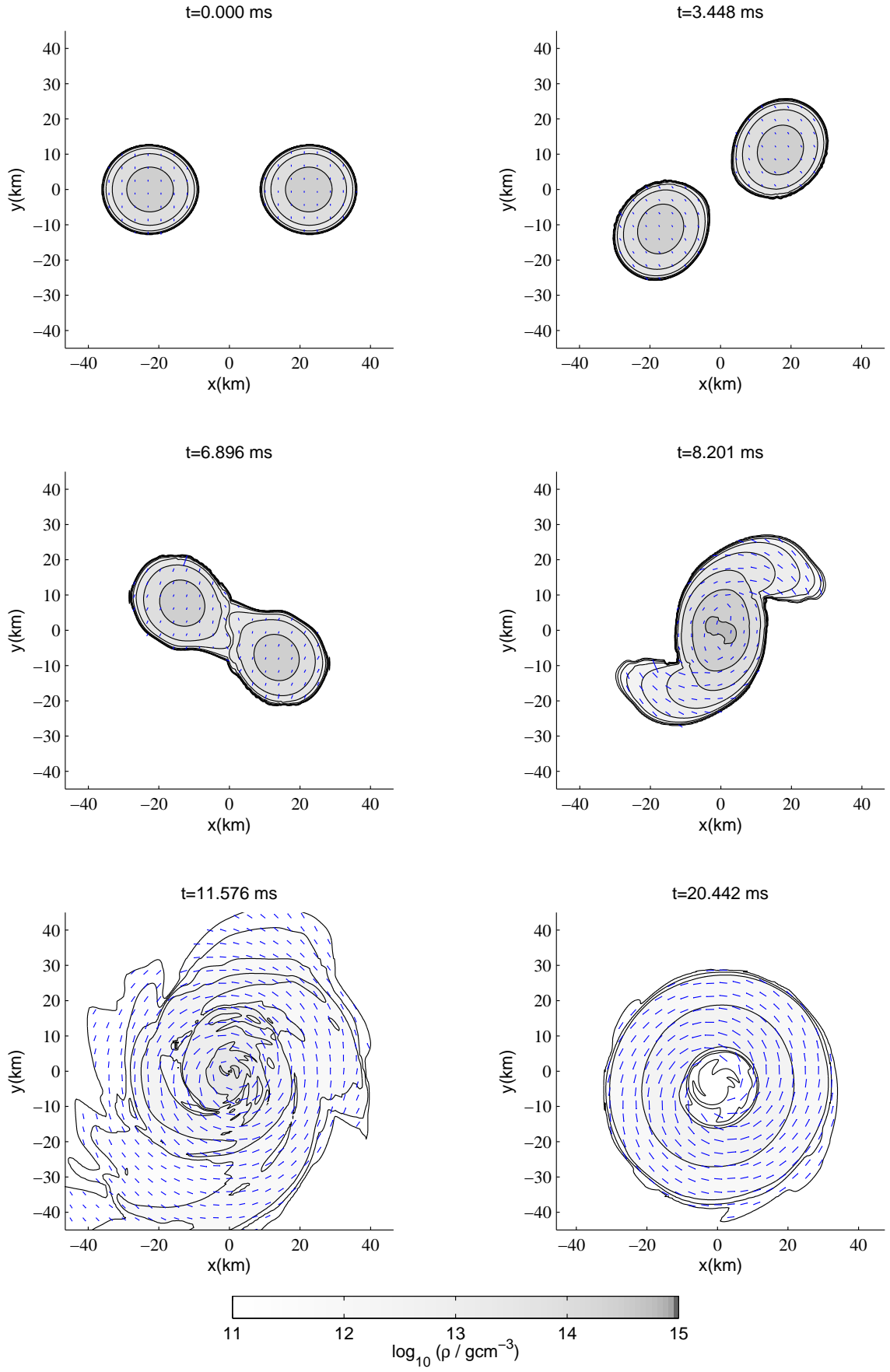
FIG. 11: Dynamics of the G2P14 evolution. The picture shows contour plots in the $x - y$ plane of the rest-mass density ρ and the velocity v^i at different times. Data refer to run H3

TABLE IV: Performances of BNS runs. Columns: grid configuration, number of processor, cpu memory, total runtime, average speed. Runs last to $t = 5000(1666\ M)$ on LRZ Munich. The numbers include LORENE initial data interpolation and checkpointing.

Grid	nproc	mem [Gb]	time [CPU hr]	speed [M/hr]
H0	32	90	192	8.7
H1	32	96	268	6.2
H2	128	120	254	6.5
H3	128	165	480	3.5

lutions of this configurations were previously performed in [22, 27]. Overall, we observe a qualitative agreement between our simulations and the results reported in the literature. Main quantitative differences are found in the post-merger phase, in particular in the collapse time of the HMNS. This is not very surprising since soon after the two stars come in contact the convergence of this kind of simulations drops to first order, e.g. [60]. The post-merger phase is thus very dependent on the resolution and grid settings employed as well as on the specific HRSC scheme employed. In the following we will mostly concentrate our discussion on G2P14 evolutions since they were performed at all the grid configurations. The G2P14hot evolutions were performed up to H1 configuration. Comparison between G2P14hot and G2P14 are presented for H1.

Fig. 11 shows contour plots in the $x - y$ (orbital) plane of the rest-mass density and the velocity field at different times of the G2P14 evolution. Data refer to run H3. The binary performs about 3 orbits before the merger. We define the merger time t_m as the peak of the (2,2) mode of the GW amplitude, $|h_{22}|$, where $h \equiv h_+ - \imath\, h_\times$ (see next section). Clearly the two stars come in contact before the merger time. From the H3 run we have $t_m = 1765$ (8.69 ms) while the contact time is about 1290 (6.3 ms). After the merger we observe a bar-shaped differentially rotating star with rest-mass $\sim 2M_b$: the HMNS [169]. Note in Fig. 11 the initial rotational symmetry of the HMNS (obtained without imposing π-symmetry in the grid) and how the symmetry is broken during the following dynamics. The large non-axisymmetric deformation of the HMNS causes a strong GWs emission [147, 148] which carries away matter angular momentum. As a result the HMNS becomes more compact and finally collapses at about $t_{AH} \sim 2118$ (10.43 ms) when an apparent horizon is first formed. A fraction of the matter remains outside the horizon and forms an accretion disk. Note that in the disk rotational symmetry is approximately restored. The mass and spin of the BH estimated from the apparent horizon are rather inaccurate due to a lack of resolution. They first rapidly grow in time reaching local maximum, then the BH mass is observed to increase (see Fig. 19) while the angular momentum decreases. We estimate at the end of the evolution $M_{BH} \sim 2.77$ and
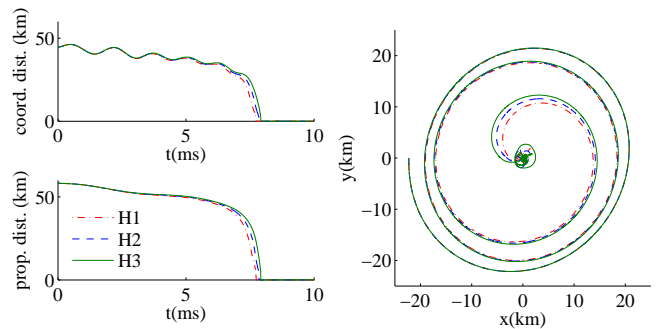

FIG. 12: Orbital motion of G2P14. The figure shows the evolution of the coordinate (top-left) and proper (bottom-left) separation of the binary and the star-track (right) of the two stars for different grid settings.

$a_{BH} \equiv J_{BH}/M_{BH}^2 \sim 0.72$. They have discrepancies of about 7% and 25% with the expected value once the gravitational radiation emission has been taken into account. Note that the collapse simulation discussed in Sec. V B, where the apparent horizon is computed with satisfactory accuracy, employs in the finest grid level a resolution about ten times higher than in the H1 runs. Additionally the gauge choice plays an important role in determining the coordinate size of the BH as discussed below.

The mesh refinement implementation is such that as soon as the two moving boxes come in contact (which happens before the contact of the two stars) a larger box with the same resolution is constructed. Before the two stars come in touch however it can happen that the boxes split back to the initial ones, evolve individually and merge again. The reason is that the evolution of a very large box is computationally not affordable in terms of memory and time. This behavior is well tested in BBH simulations [62]. It could lead to a lack of accuracy at the center of the grid but in practice it has a negligible impact since it happens when the main part of the matter is still distributed away from the center.

In the right panel of Fig. 12 we report the star-track of one of the stars, defined as the minimum of the lapse for resolutions H1, H2 and H3. The left panel instead shows for the same resolutions the coordinate (top) and proper (bottom) spatial separation. As is evident from the figure, the orbital motion has some eccentricity due to the initial data (visible in the proper separation plot) and a coordinate eccentricity (visible in the star-tracks and as oscillations in the coordinate separation) due to the evolution itself. The eccentricity of the initial data is caused by the conformally-flat approximation; the effect becomes bigger at smaller separation. In [26] the problem is corrected by adding an "approaching" radial velocity based on the post-Newtonian T4 formula. Since the procedure is constraint violating we prefer not to adopt it. The contribution to the coordinate eccentricity is mainly related to the shift condition and discussed
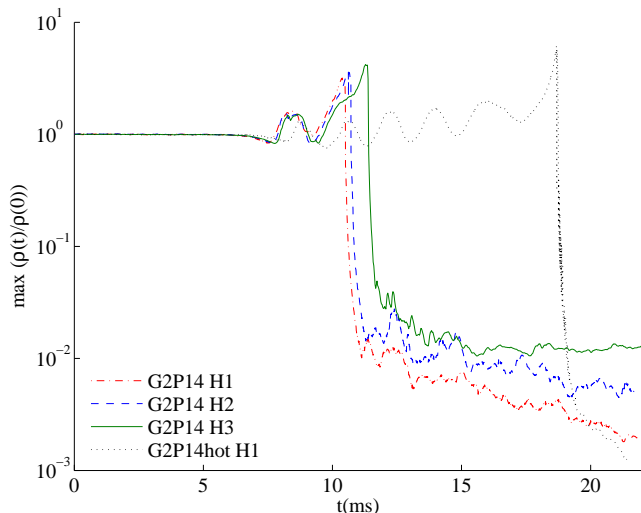
FIG. 13: Evolution of the central rest-mass density in BNS simulations. Runs G2P14 are reported for the three highest resolutions while run G2P14hot for H1.
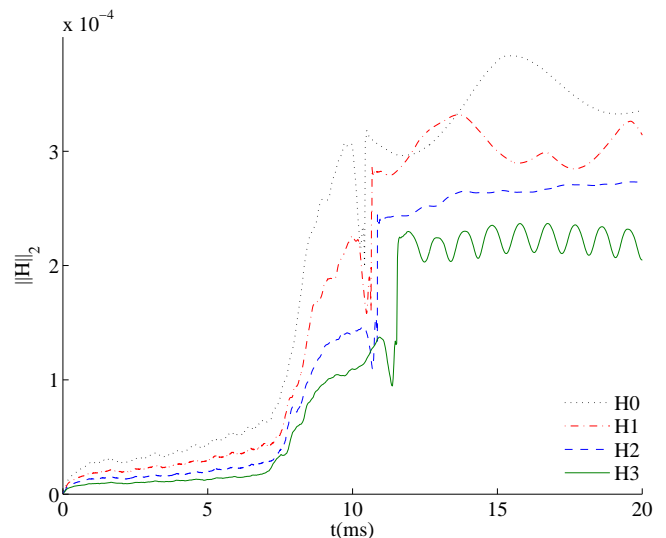

FIG. 14: Hamiltonian violation in G2P14 evolution. The figure shows the evolution of the L2 norm of the Hamiltonian constraint for different resolutions.

below. The use of a lower resolution results in an earlier merger. While the truncation errors due to finite resolution are quite large, the simulations with grid settings H have entered the "convergent regime" in the sense that we are able to estimate convergence.

The evolution of the maximum rest-mass density is shown in Fig. 13 for different resolutions. After the merger about two quasi-radial oscillations of the HMNS are observed. The maximum density increases by about a factor two indicating that the HMNS becomes more compact until, finally, it collapses. The use of more resolution results in a more persistent HMNS (see below for a comparative discussion with G2P14hot). Note the quite large differences between the runs at different resolutions. After the collapse the matter of the disk accretes onto the BH.

Concerning the constraints, the biggest violation is found in the Hamiltonian. The momentum constraint is generically one order of magnitude smaller and becomes comparable to the Hamiltonian constraint only after the formation of the "puncture". The evolution of the L2 norm of the Hamiltonian constraint is displayed in Fig. 14. The preservation of the constraint improves with resolution. We find 2nd order convergence during the whole inspiral. Most of the violation is observed in the region covered by the matter, similarly to what was discussed for the test involving a single star spacetime. After the two stars come in contact the violation rapidly increases and the convergence rate drops down to first order. At the time when an apparent horizon forms the norms show a large gradient.

The conservation of the rest-mass is excellent until the BH forms with a largest deviation of $\Delta M_0/M_0 \sim 1$ % in the H1 runs and a minimum of $\Delta M_0/M_0 \sim 0.5$ % in the H3 runs. This behavior is illustrated in Fig. 15
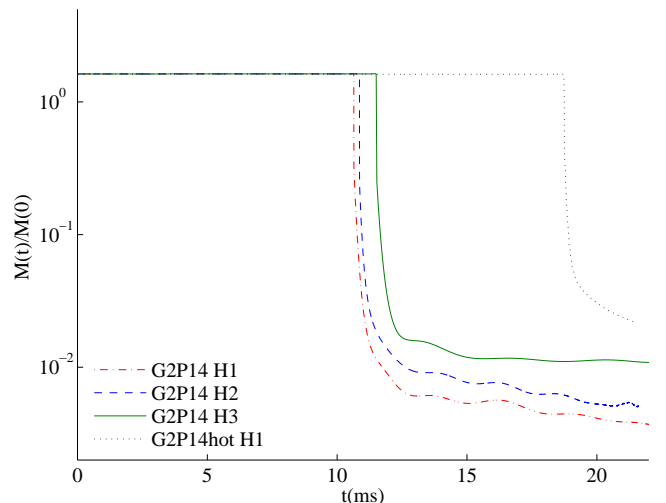

FIG. 15: Conservation of rest-mass in BNS simulations. The figure shows the evolution of the rest-mass normalized to the initial value for G2P14 and G2P14hot evolutions. Runs G2P14 are reported for the three highest resolutions, G2P14hot for resolution H1.

which displays the evolution of $\Delta M_0/M_0$. The plot shows also matter accretion after the collapse and indicates an upper limit (from run H3) for the initial rest-mass of the disk, $M_d \lesssim 2 \times 10^{-2} M_0$, since the integral in Eq. (31) is performed on the whole grid (including the BH interior).

We finally compare the dynamics of G2P14 with G2P14hot. The inspiral motion of the two binaries present small differences due to spurious numerical effects. Small errors, triggered by the artificial atmosphere treatment, propagate as simulation time advances and
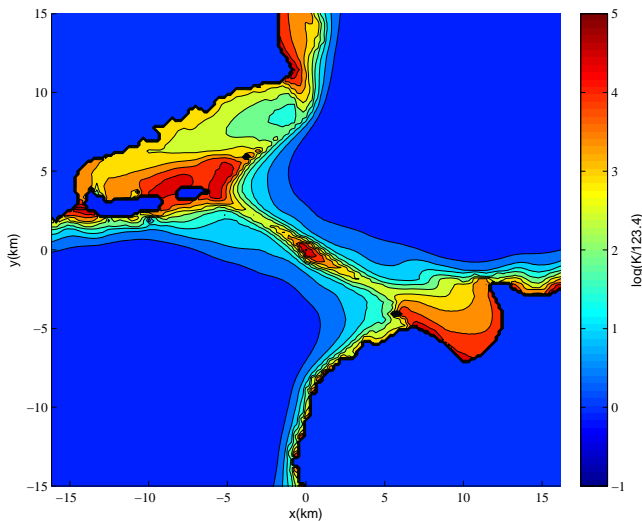
FIG. 16: Shock formation in G2P14hot evolution. The figure shows the quantity $K = p/\rho^\Gamma$ normalized by its initial value on the orbital plane at time $t = 1275$ (6.256 ms) in a $\log_{10}$ scale. Data refer to run H1.

artificially heat the stars especially at their surface. The effects of these errors on the GWs are quantified in the following section. When the two stars touch physical effects dominate instead and the evolutions significantly differ. Fig. 16 shows a contour plot in the $x - y$ plane of the quantity $K = p/\rho^\Gamma$ (normalized by its initial value) for the G2P14hot evolution. K gives a simple measure of the entropy whose variation indicates the presence of a shock (see e.g. [149] for the development of a "shock detector"), and in the G2P14 evolution K is constant by construction. In contrast, during G2P14hot evolution the inclusion of thermal effects yields shock formation when the arms of the two distorted stars come in contact. The figure shows exactly this phenomenon indicating that the quantity K increases by about 5 orders of magnitude. The thermal energy of the fluid rapidly increases reaching peaks of $\epsilon^{\rm hot} \sim 0.025 - 0.03$ corresponding to temperatures of $T \sim 2 \times 10^{11}$ K. At the time of the collapse the average temperature of the fluid is of order $T \sim 6 \times 10^{10}$ K and it has reached peaks up to $T \sim 2 \times 10^{12}$ K.

Due to the additional pressure support provided by thermal effects (see Eq. (43)) the HMNS in the G2P14hot evolution collapses later. Fig. 13 indicates that the collapse takes place after ~ 9 ms after the HMNS formation. During this time interval several quasi-radial oscillations at a frequency $\nu_{\rm F} \sim 473$ Hz and a strong GWs emission are observed (see next section). The central density shows again a drift to larger values indicating that the star is becoming progressively more compact. Results similar to G2P14 are found for what concerns rest-mass conservation as demonstrated in Fig. 15.

In [27] the evolution of G2P14 leads to a prompt collapse without the formation of a HMNS, while the evolu-

tion of G2P14hot leads to a collapse at about $t \sim 14$ ms (simulations employ the PPM implementation described in [150] and the Marquina numerical flux). In [22], where a different grid setting is employed (but the same code with the HLL numerical flux), the evolution of G2P14hot leads to a collapse at about $t \sim 16 - 17$ ms. In both works [22, 27], and differently from here, the rotational binary symmetry (π-symmetry) is enforced in the numerical grid but this procedure is expected at most to lead to a more persistent HMNS due to non-linear mode couplings (in particular $m = 1$ modes) [148]. It is thus unlikely that the grid symmetry is the reason for the discrepancy as demonstrated below. In the following we show how the HMNS dynamics is very sensitive to the numerical method employed presenting results from simulations that employ different reconstruction methods but are otherwise equivalent. Together with the low convergence of the HRSC methods in presence of turbulence [27] or shocks and given a dependence on the grid settings [60] the differences observed are not surprising.

Effect of reconstruction methods. As pointed out in Sec. V the different reconstruction methods have different truncation error magnitudes and once inserted in the algorithm produce quantitatively different results. Ref. [30] already pointed out that the use of very dissipative limiters such as MM2 can lead to very different waveforms with respect to (formally) more accurate methods while maintaining the same nominal order of convergence. Our simulations confirm this conclusion and here we show how dramatic the influence of a dissipative scheme on the dynamics can be.

We consider G2P14 evolutions at resolution H1 with the following reconstructions: MM2, MC2, PPM, CENO and CENO based on the MM2 sub-stencil (instead of the standard MC2 [109]). Since the resolution is not optimal we expect the effects due to different truncation errors to be strongly magnified. Fig. 17 shows the evolution of the maximum rest-mass density for the different methods. The vertical line marks the maximum of ρ computed from the H3 run. A visual inspection of the data is already conclusive in this case. As partially expected, the most diffusive schemes lead to an earlier merger and collapse while formally high-order reconstructions are closer to our best estimate. In the simulation with MM2 reconstruction the inspiral is very short, the HMNS is not formed and the binary evolution results in an early prompt collapse. The simulations with PPM and MC2 give similar results slightly speeding up the collapse with respect CENO. When we introduce a more dissipative component in the CENO limiter, i.e. the MM2 linear sub-stencil, the global results are significantly affected: an earlier prompt collapse is observed. The specific reason is obviously the fact that the linear sub-stencil MM2 is often selected by the limiter. We mention here that, according to our experience, MM2 reconstruction does not guarantee the long-term-stability of an equilibrium spherical star even in 1D [93].

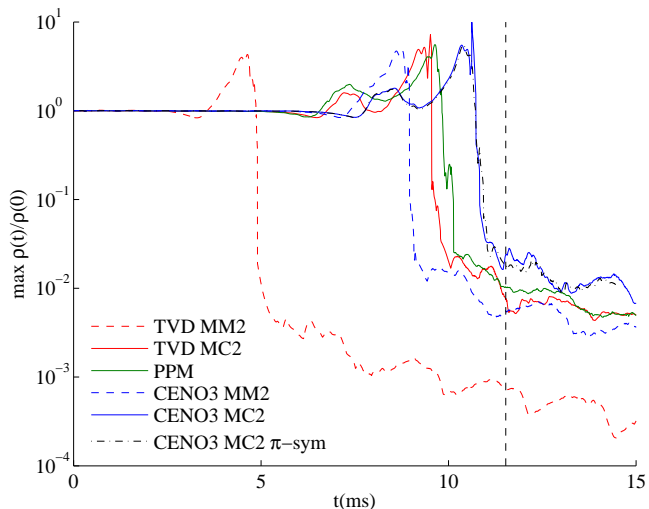Clearly the big differences shown here become progres-

FIG. 17: Dependence of the dynamics on the use of different reconstruction schemes. The figure shows the maximum of the rest-mass density obtained from G2P14 evolutions with different reconstruction methods. Reference vertical line corresponding to max ρ of run H3.

sively smaller when higher resolutions are considered. However, due to the slow (2nd) order convergence of HRSC, we expect they play a major role also at the higher resolutions employed for standard production runs. We point out that in comparing some runs with grid configurations L, M and H0 we observed a non-monotonic behavior of the results for increasing resolution. This effect seems to be related to the poor resolution but we can not exclude that the phenomenon will also happen at higher resolutions. Finally, the figure demonstrates that the use of π-symmetry does not have a relevant role (at least at this resolution) in the persistence of the HMNS as mentioned above.

Gauge study: the η parameter. Among the parameters entering the gauge conditions in Eq. (14) and Eq. (15) the damping parameter η in the Gamma-driver shift equation has been recently the subject of investigation for BBH simulations with unequal masses [151–157]. In case of equal mass BBHs it is typically set to $\eta = 1/M$ or $\eta = 2/M$, where M is the sum of the ADM masses of the two holes ($M = 1$), and it has been proved to be important to properly resolve the holes on the coordinate grid [62]. In the case of BNSs it has been suggested [112] that results are not significantly affected by this choice. Different values are adopted in the literature, e.g. $\eta = 3/M_\mathrm{b}$ [20, 112], $\eta = 1$ [27], without a detailed analysis. We demonstrate in the following that in our set up different choices of η do have an influence on the dynamics of the inspiral. In particular smaller values of η lead to a less eccentric coordinate orbital motion and to a smaller coordinate size of the final BH.

We consider G2P14 simulations with grid configuration H1 and values η = 0, 0.1, 0.3, 0.6, 0.9, 1.8,
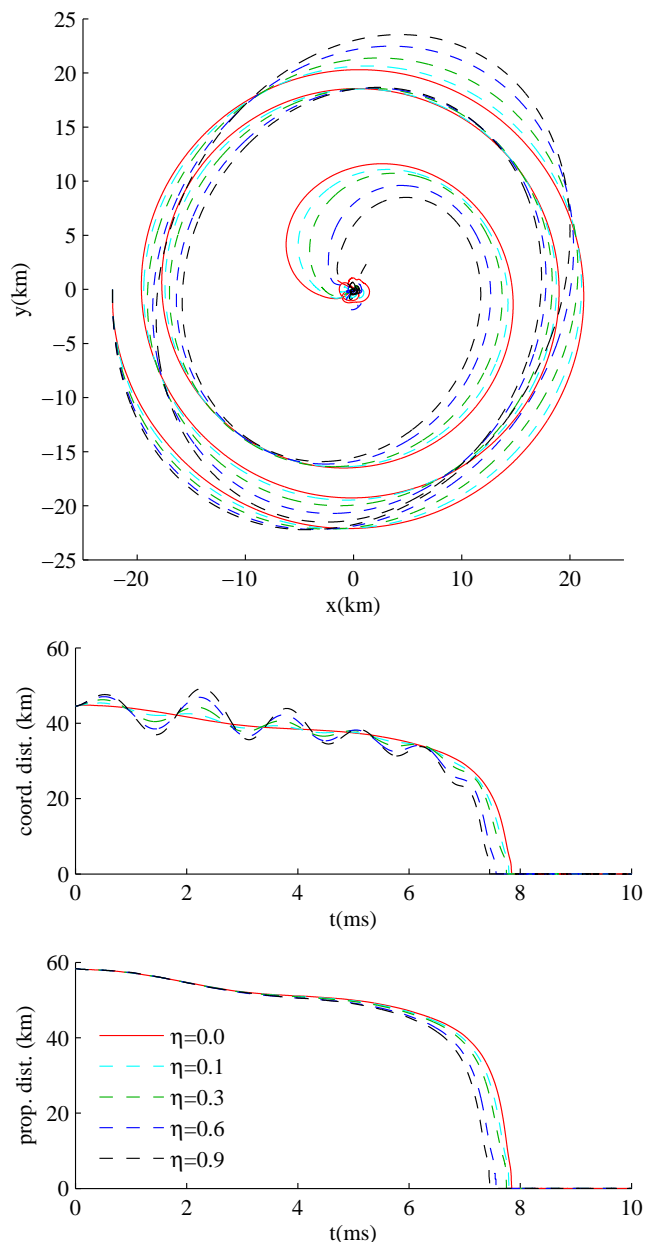

FIG. 18: Effect on orbital dynamics of different choices of the parameter η in the Gamma-driver shift condition. The top panel shows the star-track of one star. The central panel shows the evolution of the coordinate separation while the bottom panel shows the evolution of the proper separation of the binary. Each line refers to a different G2P140 evolution with a different η. Data refer to H1 runs.

i.e. $\eta \simeq 0/M$, $0.3/M$, $0.9/M$, $1.8/M$ $2.7/M$, $5.4/M$. Fig. 18 shows the star-track (top panel), the evolution of coordinate separation (central panel), and of the proper separation (bottom panel) from simulations with different values of η. The coordinate separation shows large oscillations and a systematic shift of the merger to earlier times for higher values of η. The latter is also visi-
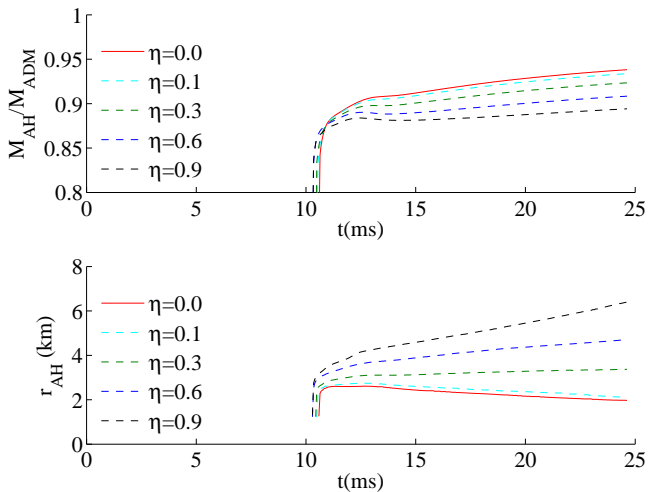
FIG. 19: Effect on the final BH mass and coordinate radius of the parameter η in the Gamma-driver shift condition. The top panel shows the irreducible mass of the final BH normalized by the ADM mass of the system as computed from the apparent horizon finder. The bottom panel shows the coordinate radius of the apparent horizon. Each line refers to a different G2P140 evolution with a different η. Data refer to H1 runs.

FIG. 20: ψ_4 waveforms from G2P14 evolution. The figure shows the real part (top panel) and the imaginary part (bottom panel) of the $r\,\psi_{22}^4$ waveform extracted at $r = 200$ from the H3 run. The amplitude is also shown in both panels.

ble in the evolution of the proper separation, which instead highlights non-circular effects due to the conformally flat initial data. The star-track shows how the coordinate eccentricity progressively reduces when smaller values of η are employed. When considering the gravitational wave emission the coordinate eccentricity does influence the extracted waves and it manifests itself in a phase difference accumulating during the inspiral. Taking as a reference the $\eta = 0$ case, the difference in the phase ϕ of $r\,\psi_{22}^4$ (see Sec. VI C) computed with $\eta = 0$ is of $\Delta\phi = 0.43, 0.90, 2.25, 3.20$ rad respectively for $\eta = 0.1, 0.3, 0.6, 0.9$ at the merger time.

Fig. 19 shows the irreducible mass, M_{AH} (normalized to the ADM mass of the system), and the coordinate radius, r_{AH}, of the apparent horizon. As expected the coordinate size of the final BH is larger for higher values of η. The choice of η must be guided by the requirement of minimizing the coordinate eccentricity of the orbital motion while keeping the ability of correctly resolving the final BH on the finest grid level. The use of $\eta = 1.8$ for example is not shown in the figure because it produces an unacceptable eccentricity in the dynamics (see Fig. 18) and the final BH has a size not completely contained in the refinement level 5, resulting in very inaccurate results. In a similar way the use of large η also affects the coordinate radius of the GW extraction spheres; smaller proper radii corresponds to higher η.
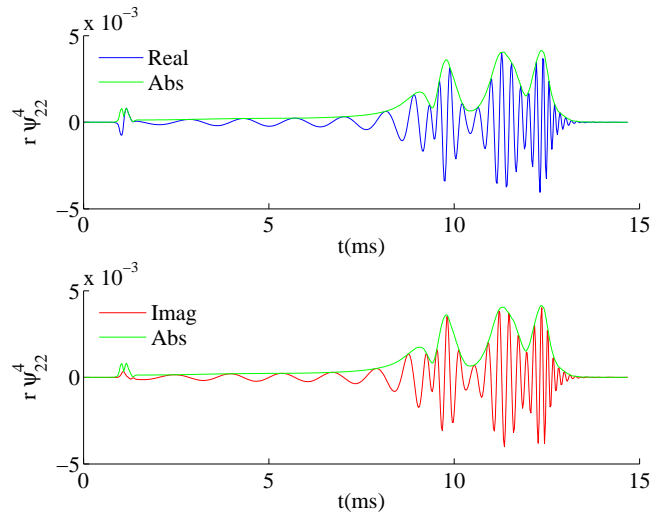
C. Gravitational waves

Gravitational radiation plays the fundamental role driving the dynamics of the binary system. GWs encode information from each phase of the evolution from the inspiral to the collapse and the BH-disk formation. We analyze in the following the GWs computed from our simulations. Again we focus the discussion on G2P14 evolution.

Our simulations show that about 1% of the initial ADM energy and 13% of the initial angular momentum are emitted in GWs during the simulation. The main emission channel is the $(\ell, m) = (2, 2)$ mode of the multipolar ($s = -2$ spin-weighted spherical harmonics) decomposition of GWs. The $(2, 2)$ mode includes about 97% of the entire radiated energy, thus we focus on the analysis of this mode. Fig. 20 shows the complex $r\,\psi_{22}^4$ waveform computed from the Newman-Penrose scalar ψ_4 as described in [62] from run H3. GWs are extracted on coordinate spheres on grid level 1. The complex waveform is usually decomposed in amplitude and phase, $r\,\psi_{22}^4 = A\exp(-\imath\phi)$. Fig. 20 shows the real (blue solid line) and the imaginary part (red dashed line) as well as the amplitude (green solid line). The extraction sphere is placed at coordinate radius $r = 200$ (295.3 km). We checked that waves extracted at different radii $r \geq 100$ show the proper fall-off behavior. The waveform is plotted against the simulated time instead of the more appropriate retarded time, see below. We present metric waveforms only with respect to the retarded time. From the plot one clearly identifies the inspiral phase followed by the emission related to the HMNS oscillations and then the collapse. At early times the well known initial
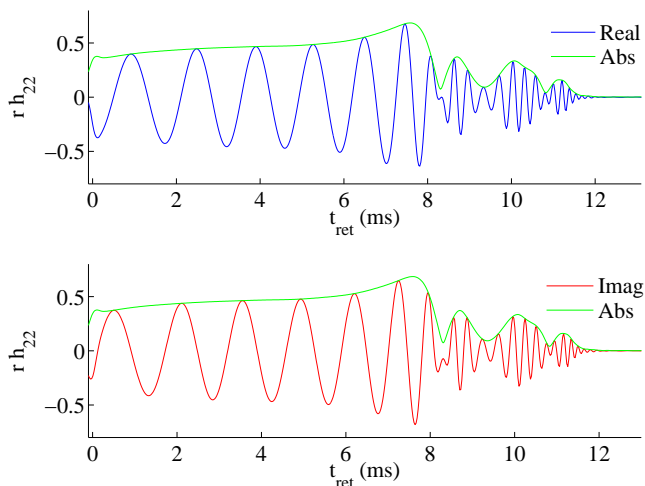
FIG. 21: Metric waveforms from G2P14 evolution. The figure shows the real part (top panel) and the imaginary part (bottom panel) of the $r\,h_{22}$ waveform extracted at $r = 200$ from H3 run. The amplitude is also shown in both panels. The waveforms are plotted versus the retarded time $t_{\rm ret} \equiv t - r_*$ where r_* is the tortoise radius corresponding to r. The metric waveform is computed with the FFI and cutoff frequency $\nu_0 = 0.002$.

"junk" radiation can be seen.

Metric waveforms. The ψ_4 waveform is the second derivative of the metric waveform $h \equiv h_+ - \imath\, h_\times$, which represents the actual GW degrees of freedom. The integration of the relation

$$\ddot{h}_{\ell\,m} = \psi_{\ell\,m}^4 \tag{59}$$

to obtain h multipoles from those of ψ_4, requires some attention. In [61, 67, 68, 158, 159] h is computed via a direct (time domain) integration on the simulated time domain. The result is affected by a polynomial drift that must be corrected by fitting. We refer to this procedure as the corrected time domain integration (CTI). The drift observed in the raw integration is not only the linear contribution expected from the integration of Eq. (59) but a generic polynomial. It originates from the integration of high-frequency noise in the data and has a stochastic nature [69]. Recently [57] an improved CTI procedure, which amounts to subtracting a post-Newtonian behavior before fitting the polynomial correction, which we did not consider here, has been developed. In [69] the fixed-frequency integration (FFI) method has been proposed. It is based on a spectral integration in the Fourier basis and employs a simple high-pass frequency filter against spectral leakage.

We computed h_{22} with both the CTI and the FFI procedure finding comparable results. Differences are discussed below. We focus for the moment on h_{22} computed with FFI: the integration method does not influence the following statements. Fig. 21 shows the metric waveform $r\,h_{22}$ computed from $r\,\psi_{22}^4$ as a function

of the retarded time $t_{\rm ret} \equiv t - r_*$ where $r_* \simeq 222$ is the tortoise radius [170] corresponding to $r = 200$. Real part, imaginary part and amplitude are shown for run H3. The peak of the amplitude of h_{22} formally defines the merger time, $t_{\rm m}$, e.g. [57, 160]. Considering different resolutions we found $t_{\rm m} = 1670, 1710, 1740$ and 1765 (8.23, 8.42, 8.57 and 8.69 ms), respectively, for runs H0-3. The corresponding retarded times are $t_{\rm m,ret} = 1446, 1486\,1516, 1541$ (7.12, 7.32, 7.47, 7.59 ms). The metric waveform is composed at early times of six GW cycles emitted during the three orbit inspiral. After the merger the emission is dominated by the bar-deformed HMNS, and the signal has a typical frequency around 3 kHz which increases as the HMNS becomes more compact [135, 161]. Finally, after $t_{\rm ret} > 2132$ (10.5 ms) the GW signal is composed of the quasi-normal-mode ringing of the BH. We observe from the waves the fundamental frequency $\nu_{\rm QNM} \sim 6.5$ kHz, compatible with the estimate of the BH mass and spin from the apparent horizon [27, 162], i.e. $\nu_{\rm QNM} \sim 3.23(10/M_{\rm BH})[1 - 0.63(1 - a_{\rm BH})^{0.3}]$. The value $\nu_{\rm QNM}$ can be estimated by fitting the plateau of the GW frequency when it reaches its absolute maximum (see Fig. 24). A better estimate is provided by the frequency of the ψ_4 waveforms because the signal is less noisy and not contaminated by the integration procedure.

We comment now on the two integration methods employed in the post-processing of ψ_4 to obtain h. In the FFI we use as cut off frequency the value $\nu_0 = 0.002$ (406 Hz), slightly below the GW frequency of the initial data. The polynomial correction employed in the CTI is a 3rd order polynomial. This choice is preferred against a linear or quadratic correction since it minimizes experimentally the drift in the raw integrated waveforms and the oscillations in the modulus (see below). The phase difference between the two metric waveforms amounts to $\Delta\phi \lesssim 0.06$ from early times until the collapse. This value is very small and can be considered insignificant (see error estimates below and Tab. V). On the other hand the amplitudes do differ in a relevant way. The relative difference is less than $\Delta A/A < 5\%$ during the inspiral and grows to about 15% before the collapse. While these numbers do not seem dramatic another important effect is observed. Fig. 22 shows the amplitude of $r\,h_{22}$ computed with the two methods: solid red line for FFI and dashed blue line for CTI. The amplitude computed with the CTI shows oscillations during the inspiral. These oscillations converge away considering higher resolutions but we were not able to remove them completely (the oscillation amplitude is larger in waveforms from lower resolutions runs). Waves extracted at larger extraction radii show smaller oscillations. The use of a linear polynomial correction results in very large oscillations (black dotted line) and a prominent drift in the waveforms. By contrast the amplitude obtained by the FFI waveform integrated with $\nu_0 = 0.002$ is free from these oscillations for all the resolutions considered. When the FFI with a much lower cutoff frequency,
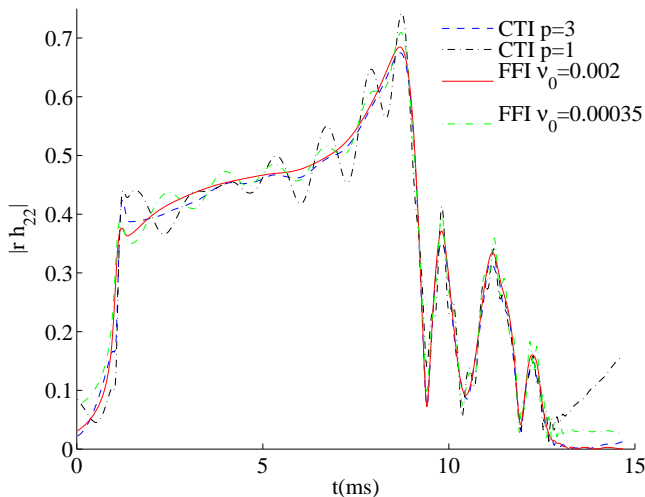
FIG. 22: Gravitational wave amplitude $|r\,h_{22}|$ from G2P14 evolution. The figure shows the amplitude computed with the FFI $\nu_0 = 0.002$ (red solid line) and $\nu_0 = 0.00035$ (green dashed-dotted line) and with the CTI where a cubic (blue dashed line) and linear polynomial (black dotted line) correction is used.
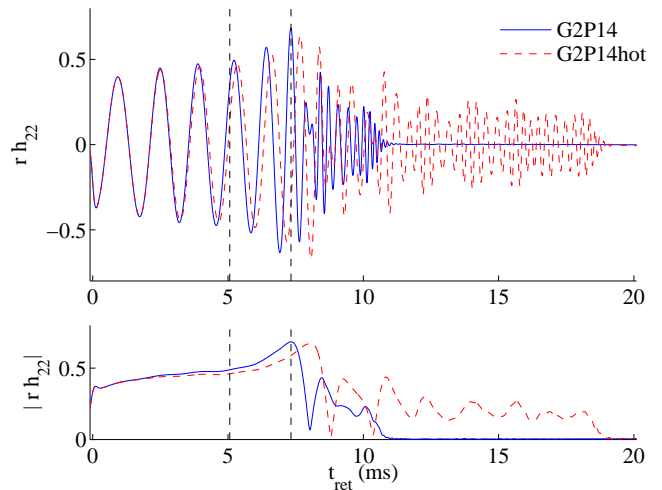

FIG. 23: Comparison between waveforms from G2P14 and G2P14hot evolutions. The top panel shows the real part of h_{22} extracted at $r = 200$ for the two evolutions. The bottom panel shows the amplitudes. Vertical lines mark the time of the first contact between the stars and the merger time for G2P14 evolution. The waveforms are plotted against the retarded time $t_{ret} \equiv t - r_*$. Data refer to run H1.

$\nu_0 = 0.00035$ (71 Hz), is employed the oscillations appear again (green dashed-dotted line). Note that a frequency of 71 Hz roughly corresponds to the finite length of the signal. As observed in [67, 69] the oscillations are an unphysical effect not related to eccentricity. We mention however that we find here a correlation between the oscillations in the amplitude of $r\,h_{22}$ and those seen in the coordinate separation (Fig. 18) in the runs with different values η. A gauge effect on the extraction spheres amplified in the calculation of h is thus a possible explanation. A proper choice of ν_0 in the FFI can mostly eliminate them, while polynomial fitting in CTI is not as robust and not performing as well for our data.

Thermal effects. We discuss now differences between the waveforms produced in G2P14 and G2P14hot evolution. The results refer to H1 runs and they are discussed referring to Fig. 23. As discussed in Sec. VI B the simulations show differences of numerical origin already in the inspiral. The phase difference between the h_{22} waveforms increases monotonically during the evolution until $t_{ret} \sim 12$ ms when the emission of G2P14 is practically zero. At the time the two stars experience the first contact the G2P14hot h_{22} waveform has accumulated a dephasing of $\Delta\phi = +0.67$ rad and the amplitude is about 6 % smaller. Since these differences are compatible with the truncation errors for this resolution and they are not expected in the continuum limit (the inspiral is an isentropic process from the fluid point of view) they likely have a numerical origin. After the contact, thermal effects drive a very different dynamics compared to the isentropic case as discussed in Sec. VI B (see Fig. 16). The dephasing reaches $\Delta\phi = +2.11$ rad at

the merger time and the amplitude is about 14 % smaller. Similarly for the $r\,\psi_{22}^4$ waveform we found a dephasing of $\Delta\phi = +0.67$ rad and a factor -15 % in amplitude at the contact time and a dephasing of $\Delta\phi = +2.43$ rad and a factor -50 % in amplitude at the merger time. The postmerger emission in the G2P14hot evolution is dominated by the emission of the bar-deformed HMNS. A lower frequency modulation of the signal is visible in the amplitude of the waveform and corresponds to the nonlinear quasi-radial pulsations shown in Fig. 13 and previously discussed. The high-frequency part of the GW signal is instead dominated by $m = 2$ non-axisymmetric nonlinear modes and it is composed of few frequencies around 2.7 kHz. A Fourier analysis shows results qualitatively compatible with [163].

A relevant quantity directly connected to the dynamics of the system is the GW frequency defined as $\omega_{22} \equiv -\Im(\dot{h}_{22}/h_{22})$, i.e. the derivative of the GW phase. Fig. 24 displays the dimensionless $M\,\omega_{22}$ as computed from G2P14 and G2P14hot evolutions. During the inspiral the GW frequency increases monotonically from $M\,\omega_{22} \sim 0.056$ to $M\,\omega_{22} \sim 0.126$. This value (green horizontal solid line, see the bottom panel) is common to both evolutions but occurs at different times due to the accumulated phase. After the merger, a first local maximum is observable with again very close values for G2P14 ($M\,\omega_{22} \sim 0.181$) and G2P14hot ($M\,\omega_{22} \sim 0.184$) and different times ($t_{ret} \sim 7.84$ ms for G2P14hot and $t_{ret} \sim 8.68$ ms for G2P14hot). The GW frequencies present the same behavior until this point, thermal effects generate only a time shift (retardation). After the merger, the GW

frequency of G2P14 presents one oscillation and increases from $M\,\omega_{22} \sim 0.2$ to $M\,\omega_{22} \sim 0.245$ when the apparent horizon forms. With a steep gradient it further increases to $M\,\omega_{22} \sim 0.57$ which correspond to the fundamental QNM of the Kerr BH ($\nu_{\rm QNM} \sim 6.5$ kHz). In the case of G2P14hot the GW frequency reflects the dynamics of the HMNS: it increases almost linearly with large oscillations corresponding to the HMNS quasi-radial oscillations. After the local minimum of the last oscillation the collapse happens at a frequency $M\,\omega_{22} \sim 0.27$. The QNM frequency on the G2P14hot evolution is slightly below the corresponding isentropic evolution, $\nu_{\rm QNM} \sim 6.45$ kHz. Interestingly the GW frequency becomes negative after the first local maximum after the merger in both evolutions and one oscillation later in G2P14hot (after the formation of the apparent horizon in the G2P14 evolution). It is difficult to say if these features have a physical or a numerical origin. However, the GW frequency zeros and negative spikes, roughly correspond to times at which the distribution of the rest-mass density in the equatorial plane is almost-spherical. Note in addition that the amplitude of the GWs drops to zero (bottom panel of Fig. 23).

Convergence. We discuss now convergence of the waveforms produced in G2P14 evolutions and runs H1, H2 and H3. The real part of $r\,\psi_{22}^4$ is reported in Fig. 25 for the different runs. The convergence study is focused on the inspiral part of the wave. Similar results are found for the series H0, H1 and H2, with larger absolute errors.

Fig. 26 displays the (logarithmic) differences between the $r\,\psi_{22}^4$ amplitude (top panel) and phase (bottom panel). The difference between H2 and H3 scaled for second order convergence is also plotted. The vertical line in the figure marks the merger time as computed from the waveforms extrapolated in resolution. The initial junk radiation is also cut out from the figure. We observe a quite clear 2nd order convergence in the amplitude while for the phase the convergence appears slower. The phase error is also the dominating error in the waveforms at different resolutions. A direct inspection of Fig. 25 already highlights this fact. The experimental convergence rate measured for the phase is a factor between 1 and 2, which suggests that the simulations have "just entered" a convergent regime but more resolution or higher order numerical methods are required. A proper time shift of the waveforms may locally eliminate the phase error thus improving the results. We prefer not to perform such procedure in order to keep the analysis simple and clean. The practice of aligning waveforms for convergence tests has been abandoned in some BBH simulations even in the more complicated cases of unequal masses and spins, see e.g. [59, 152, 164].

Convergence in the waveforms is lost soon after the merger. In the post-merger phase a first order in norm convergence is observed in several global quantities, cf. Fig. 14 and the discussion in the previous section. From our data it is not possible to estimate a precise point-wise convergence rate in the waveforms: the
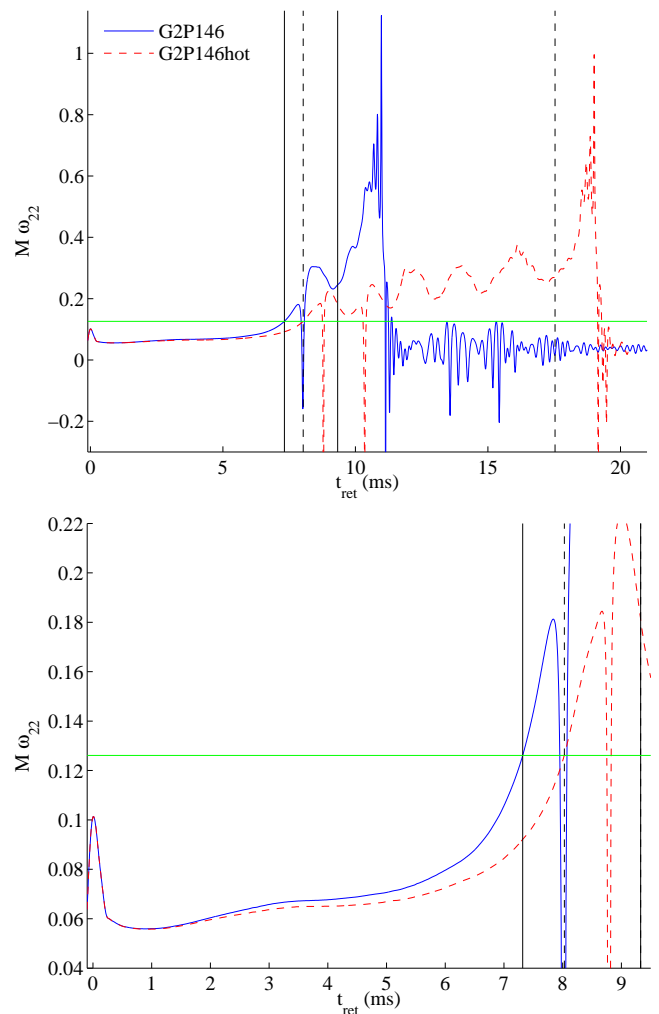

FIG. 24: Gravitational wave frequency from G2P14 and G2P14hot evolutions. The figure shows $M\,\omega_{22}$ computed from h_{22} waveforms. In the top panel the blue solid line refers to G2P14 and the red dashed line to G2P14hot. The vertical black solid lines mark respectively the merger time and the apparent horizon formation for G2P14. The vertical black dashed lines mark respectively the merger time and the apparent horizon formation for G2P14hot. The bottom panel gives a detail of the top panel showing the inspiral part. The horizontal green solid line marks the value of $M\,\omega_{22}$ at the merger for G2P14. Data refer to run H1.

convergence in amplitude smoothly drops down to first order, the phase shows over-convergence. We observe however a monotonic dependence on resolution as evident from Fig. 25. The reason for this behaviour is again the truncation error of the HRSC scheme in this strongly nonlinear hydrodynamical phase (characterized by a rapid variability in space and time) which dramatically affects the waveforms.

Using the Richardson method we extrapolate the inspiral waveforms in order to estimate errors in amplitude and phase. Results concerning the maximum error esti-
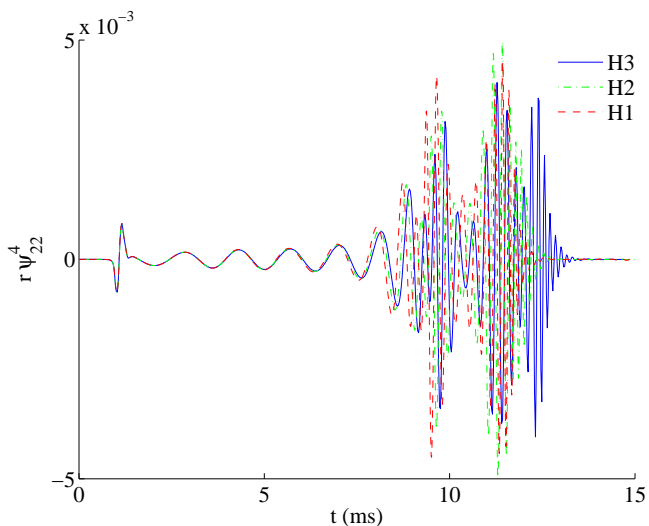
FIG. 25: ψ_4 waveforms from G2P14 evolution at different resolutions. The figure shows the real part of the $r\,\psi_{22}^4$ waveform extracted at $r = 200$ from runs H1-3.

mated during the inspiral are reported in Tab. V. Using the four resolutions and assuming 2nd order convergence, we obtain ψ_4 waveforms with a maximum phase error of $\max \delta\phi \sim 0.3$ rad and $\max \delta A/A \sim 7$ %. Assuming 1st order convergence gives instead $\max \delta\phi \sim 1$ rad and $\max \delta A/A \sim 24$ %. Similarly using only the three highest resolutions gives $\max \delta\phi \sim 0.6$ rad and $\max \delta A/A \sim 14$ % for 2nd order and $\max \delta\phi \sim 1.2$ rad but an unacceptable amplitude error for the 1st order assumption. The errors on the metric waveform are comparable while generically smaller. Furthermore we note that the assumption of 1st order convergence leads to an evidently non realistic estimate of the merger time from the extrapolated data $t_{\rm m} = 2280$ (11.23 ms) (H1-3 data) while it gives a more reasonable $t_{\rm m} = 1800$ (8.87 ms) for 2nd order (H1-3 data).

Some care is needed in interpreting these results because of the previous discussion. However, from our results we conclude that: (i) the series H0-2 while showing convergence is too inaccurate and not reliable for error estimates; (ii) assuming 1st order convergence for the series H1-3 and H0-3 is not appropriate and overestimates the actual errors; (iii) a conservative and realistic error estimate is provided by H1-3 data assuming 2nd order convergence; (iv) the error on the extrapolated data can be estimated as the difference between the extrapolation with four resolutions (H0-3) and three resolutions (H1-3), e.g. $\max \delta\phi \sim 0.33$ rad and $\max \delta A/A \sim 7.4$ % for $r\,\psi_{22}^4$. As indicated in [57], the main error on the waveforms is due, as expected, to resolution rather than finite radius extraction. Since our results are clearly dominated by truncation error we did not investigate finite extraction errors but left that study for future work.
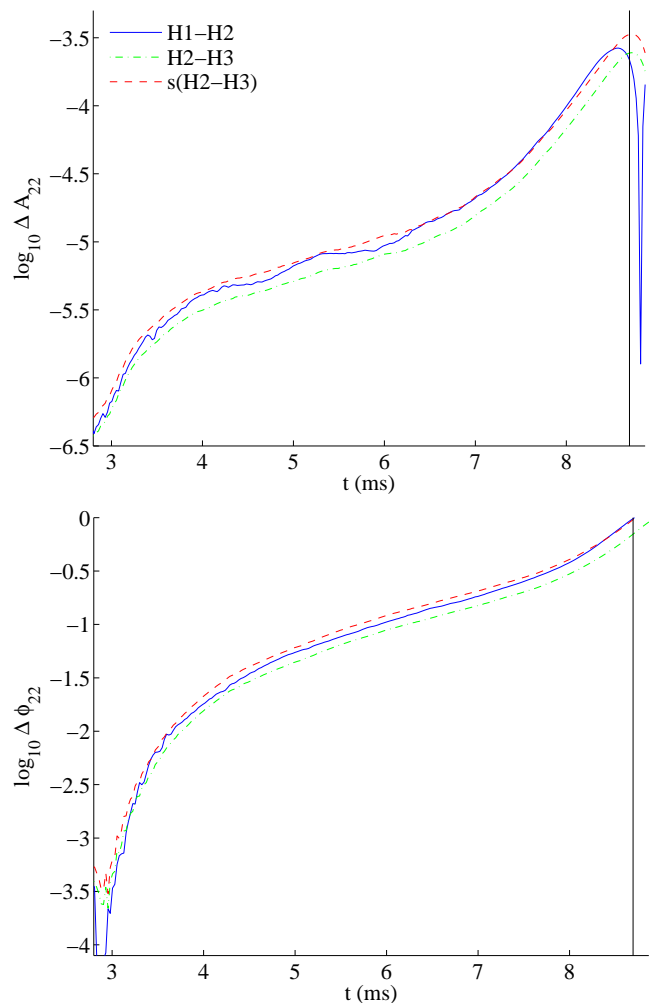

FIG. 26: Convergence of phase and amplitude in $r\,\psi_{22}^4$ waveform from G2P14 evolution. The figure shows the difference between runs H1 and H2 (blue solid line), between runs H2 and H3 (green solid-dotted line) as well as the difference between H2 and H3 (red dashed line) scaled for 2nd order convergence. Top panel displays the logarithm of amplitude differences, bottom panel displays the logarithm of phase differences. The vertical line indicates the merger.

VII. CONCLUSIONS

In this work we presented detailed tests and first full scale evolutions for a new computer code aimed at 3+1 numerical studies of general relativistic matter spacetimes. The implementation represents an upgrade of the BAM code developed previously for vacuum systems [62–64]. The code solves the flux-conservative formulation of the GRHD equations [65] coupled with the BSSNOK system. Mesh refinement (moving boxes) and a metric solver were already provided by the BAM code. The GRHD equations are solved by means of robust HRSC methods [94, 96–99] and share the same grid and the same time stepping algorithm with the metric solver. We de-

TABLE V: Error estimates during inspiral for extrapolated waveforms. Columns: data used for extrapolation, assumed order of convergence, waveform, maximum absolute error in phase, maximum relative error in phase, maximum relative error in amplitude.

data	r	waveform	max $\delta\phi$ [rad]	max $\delta\phi/\phi$ [%]	max $\delta A/A$ [%]
H0-3	2	$r\,\psi_{22}^4$	0.29	0.68	6.89
		$r\,h_{22}$	0.26	0.64	2.65
	1	$r\,\psi_{22}^4$	1.04	2.40	24.02
		$r\,h_{22}$	0.87	2.17	13.31
H1-3	2	$r\,\psi_{22}^4$	0.62	1.43	14.30
		$r\,h_{22}$	0.53	1.32	6.85
	1	$r\,\psi_{22}^4$	1.20	2.85	$\gtrsim 100$
		$r\,h_{22}$	1.10	2.81	$\gtrsim 100$

scribed in detail the equations and the numerical method implemented. The code allows the use of one-parameter EoS tables and implements the hybridization procedure of [36] to model thermal effects. We proposed a simple, thermodynamically consistent interpolation scheme for one-parameter EoSs.

We validated the code against a number of stringent tests involving single star spacetimes. We studied the performance of different reconstruction procedures and the convergence of the code. We found that in our set up the use of CENO reconstruction shows a clear 2nd order convergence and leads to smaller global truncation errors compared to the other methods.

We presented test evolutions of irrotational equal-mass binary neutron star configurations. Matter is described by simple polytropic and ideal gas EoSs. In both evolutions the formation of an HMNS is observed. In the isentropic case it collapses quite rapidly producing a Kerr BH surrounded by a disk of mass $M_{\rm d} \lesssim 2 \times 10^{-2} M_0$ while in the other case the HMNS survives for 9 ms due to thermal pressure support.

We investigated the impact of different reconstruction methods on the dynamics of the HMNS. Our results highlight a strong influence of the numerical method and of the resolution on the simulated physics. Precise quantitative statements on the post-merger phase require extreme care.

We presented new results concerning the use of different values of the damping parameter η in the shift condition. Small values of η are found to produce a less coordinate-related eccentricity during inspiral and to reduce the coordinate size of the final BH.

The gravitational radiation emitted by the system was investigated. We characterized the GWs (metric waveforms) and discussed two different methods to compute them from ψ_4 waveform: a time domain (CTI, e.g. [67, 68]) and Fourier domain (FFI, [69]) integration. The FFI provides better results minimizing unphysical drifts and oscillations. We performed self-convergence tests of the waveforms. While the resolutions employed

are probably close but not still not optimal for production runs, we found 2nd order convergence during the inspiral phase without any time-shifting procedure. For the first time in BNS simulations we consistently estimated error-bars on the waveforms by extrapolating the results in resolution.

This work represents our first contribution to the study of GWs from BNS systems. The methodology presented here will be applied in future works. In particular, we plan in the near future the production of accurate and convergent inspiral waveforms from initial configurations described by different realistic EoS in order to investigate the impact of the EoS on the GW signal [6, 54, 56, 57].

Appendix A: Algorithm to recover primitives

In this appendix we summarize the procedure and the equations to recover the primitive variables from the conservative ones. The specific algorithm adopted has been developed in a number of previous publications [23, 106, 110, 120, 136, 165]. Other algorithms have been developed, e.g. [166, 167], in particular we have successfully tested the method of [166] in single star evolutions. We leave for future work extensive tests and comparisons between different algorithms.

We first discuss an iterative procedure for a general EoS, $p = P(\rho, \epsilon)$, first employed in [165]. Specific procedures can be designed once a specific form of EoS is given [92]. We then present the procedure we adopt in the case of cold EoSs which is based on an iterative algorithm for ρ [110]. Finally we describe the modifications introduced to handle the presence of the artificial atmosphere.

Following [106] we invert Eqs. (22) to find

$$v^i(p) = \frac{S^i}{\tau + D + p} , \tag{A1}$$

$$W(p) = \frac{\tau + p + D}{\sqrt{(\tau + p + D)^2 - S^2}} , \tag{A2}$$

$$\rho(p) = \frac{D}{W} , \tag{A3}$$

$$\epsilon(p) = D^{-1}\left[\sqrt{(\tau + p + D)^2 - S^2} - Wp - D\right] \tag{A4}$$

Primitive variables can be computed from the conservative variables using the above relations once the pressure is known. The pressure is determined by the EoS looking for the root of the nonlinear algebraic equation

$$f(p) \equiv p - P\left(\rho(p), \epsilon(p)\right) = 0 . \tag{A5}$$

The algorithm used is the Newton-Raphson iteration,

$$p^{\mathrm{new}} = p^{\mathrm{old}} - \frac{f(p)}{f'(p)} . \tag{A6}$$

The derivative of f is given by

$$f'(p) = 1 - \chi\frac{\partial\rho}{\partial p} - \kappa\frac{\partial\epsilon}{\partial p} , \tag{A7}$$

$$\frac{\partial\rho}{\partial p} = \frac{DS^2}{(D + p + \tau)^2\sqrt{(D + p + \tau)^2 - S^2}} , \tag{A8}$$

$$\frac{\partial\epsilon}{\partial p} = \frac{pS^2}{D\left((D + p + \tau)^2 - S^2\right)^{3/2}} . \tag{A9}$$

In the case of a one-parameter EoS, $p = P(\rho)$, $h = h(\rho)$, $\epsilon = \epsilon(\rho)$, and

$$W = \sqrt{1 + \frac{S^2}{(Dh)^2}} \tag{A10}$$

are functions of the density and the conservative variables only. Primitive variables can be computed from ρ, once the latter is determined by

$$g(p) = W(\rho)\rho - D , \tag{A11}$$

using again a Newton-Raphson root finder with

$$g'(\rho) = W(\rho) - \rho\frac{S^2 h'(\rho)}{WD^2 h^3} , \tag{A12}$$

$$h'(\rho) = \epsilon'(\rho) - \frac{P}{\rho^2} + \frac{\chi}{\rho} . \tag{A13}$$

Note that $h'(\rho) = \frac{\chi}{\rho}$ if the principle of thermodynamics at zero temperature is applied.

The recovery procedure for a general EoS can fail at low densities, e.g. in presence of the atmosphere. A reason for this is simply machine accuracy: since typically $p \ll D$, for very low densities the Newton-Raphson algorithm does not converge. A further complication is the spuriously high value of the velocity generated by the artifical atmosphere treatment. To handle these problems, similarly to [23, 110], we combine both the algorithms described above and we implement a set of hierarchic prescriptions which are found to work in practice. Specifically: (i) every time a grid point reaches a density below the atmosphere threshold density the code sets atmosphere values both in primitives and conservatives and continues to the next point; (ii) if the general EoS algorithm does not converge due to a too small value of the pressure, i.e. $p^{\mathrm{new}} - p^{\mathrm{old}} < \varepsilon \sim 10^{-12}$, then atmosphere values are set; (iii) if it returns unphysical values for ϵ, ρ or p then the code tries the inversion with the algorithm for the cold EoS; (iv) if it returns unphysical values of v^2 then atmosphere values are set; (v) if the algorithm for the cold EoS does not converge or returns unphysical values not cured by finer grid levels, then the code stops. In practice we observe the necessity of (ii), (iii) and (iv) only in binary simulations.

[1] K. Belczynski, V. Kalogera, F. A. Rasio, R. E. Taam, and T. Bulik, Astrophys. J. **662**, 504 (2007), astro-ph/0612032.

[2] N. Andersson et al., Gen. Rel. Grav. **43**, 409 (2011), 0912.0384.

[3] J. Abadie et al. (LIGO Scientific), Class. Quant. Grav. **27**, 173001 (2010), 1003.2480.

[4] W. H. Lee and E. Ramirez-Ruiz, New J. Phys. **9**, 17 (2007), astro-ph/0701874.

[5] E. Nakar, Phys. Rept. **442**, 166 (2007), astro-ph/0701748.

[6] J. S. Read et al., Phys. Rev. **D79**, 124033 (2009), 0901.3258.

[7] S. Rosswog and M. B. Davies, Mon. Not. Roy. Astron. Soc. **345**, 1077 (2003), astro-ph/0110180.

[8] S. Rosswog, E. Ramirez-Ruiz, and M. B. Davies (2003), astro-ph/0306418.

[9] L. Rezzolla et al. (2011), 1101.4298.

[10] B. Paczynski, Astrophys. J. **308**, L43 (1986).

[11] R. Narayan, B. Paczynski, and T. Piran, Astrophys. J. **395**, L83 (1992), astro-ph/9204001.

[12] J. Faber, Classical and Quantum Gravity **26**, 114004 (2009), URL http://stacks.iop.org/0264-9381/26/i=11/a=114004.

[13] M. D. Duez, Class. Quant. Grav. **27**, 114002 (2010), 0912.3529.

[14] S. Rosswog (2010), 1012.0912.

[15] M. Shibata and K. Uryu, Phys. Rev. **D61**, 064001 (2000), gr-qc/9911058.

[16] F. Pretorius, Phys. Rev. Lett. **95**, 121101 (2005), gr-qc/0507014.

[17] J. G. Baker, J. Centrella, D.-I. Choi, M. Koppitz, and J. van Meter, Phys. Rev. Lett. **96**, 111102 (2006), gr-qc/0511103.

[18] M. Campanelli, C. O. Lousto, P. Marronetti, and Y. Zlochower, Phys. Rev. Lett. **96**, 111101 (2006), gr-qc/0511048.

[19] M. Anderson et al., Phys. Rev. **D77**, 024006 (2008), 0708.2720.

[20] T. Yamamoto, M. Shibata, and K. Taniguchi, Phys. Rev. **D78**, 064054 (2008), 0806.4007.

[21] Y. T. Liu, S. L. Shapiro, Z. B. Etienne, and K. Taniguchi, Phys. Rev. **D78**, 024012 (2008), 0803.4193.

[22] B. Giacomazzo, L. Rezzolla, and L. Baiotti, Phys. Rev. **D83**, 044014 (2011), 1009.2468.

[23] J. A. Font, M. A. Miller, W.-M. Suen, and M. Tobias, Phys. Rev. **D61**, 044011 (2000), gr-qc/9811015.

[24] J. A. Font et al., Phys. Rev. **D65**, 084024 (2002), gr-qc/0110047.

[25] M. A. Miller, P. Gressman, and W.-M. Suen, Phys. Rev. **D69**, 064026 (2004), gr-qc/0312030.

[26] K. Kiuchi, Y. Sekiguchi, M. Shibata, and K. Taniguchi, Phys. Rev. **D80**, 064037 (2009), 0904.4551.

[27] L. Baiotti, B. Giacomazzo, and L. Rezzolla, Phys. Rev. **D78**, 084033 (2008), 0804.0594.

[28] L. Rezzolla, L. Baiotti, B. Giacomazzo, D. Link, and J. A. Font, Class. Quant. Grav. **27**, 114105 (2010), 1001.3074.

[29] M. Anderson et al., Phys. Rev. Lett. **100**, 191101 (2008), 0801.4387.

[30] B. Giacomazzo, L. Rezzolla, and L. Baiotti, Mon. Not. Roy. Astron. Soc. **399**, L164 (2009), 0901.2722.

[31] C. Palenzuela, L. Lehner, O. Reula, and L. Rezzolla (2008), 0810.1838.

[32] T. Nakamura, K. Oohara, and Y. Kojima, Prog. Theor. Phys. Suppl. **90**, 1 (1987).

[33] M. Shibata and T. Nakamura, Phys. Rev. **D52**, 5428 (1995).

[34] T. W. Baumgarte and S. L. Shapiro, Phys. Rev. **D59**, 024007 (1999), gr-qc/9810065.

[35] L. Lindblom, M. A. Scheel, L. E. Kidder, R. Owen, and O. Rinne, Class.Quant.Grav. **23**, S447 (2006), gr-qc/0512093.

[36] M. Shibata, K. Taniguchi, and K. Uryu, Phys. Rev. **D71**, 084021 (2005), gr-qc/0503119.

[37] A. Bauswein, H. T. Janka, and R. Oechslin (2010), 1006.3315.

[38] M. H. Ruffert, H. T. Janka, and G. Schaefer, Astron. Astrophys. **311**, 532 (1996), astro-ph/9509006.

[39] M. Ruffert, H. T. Janka, K. Takahashi, and G. Schaefer, Astron. Astrophys. **319**, 122 (1997), astro-ph/9606181.

[40] R. Oechslin and H. T. Janka, Phys. Rev. Lett. **99**, 121102 (2007), astro-ph/0702228.

[41] K. S. Thorne, Mon. Not. Roy. Astron. Soc. **194**, 439 (1981).

[42] Y. Sekiguchi, Prog. Theor. Phys. **124**, 331 (2010), 1009.3320.

[43] Y. Sekiguchi (2010), 1009.3358.

[44] Y. Sekiguchi, K. Kiuchi, K. Kyutoku, and M. Shibata (2011), 1105.2125.

[45] M. Shibata and K. Uryu, Phys. Rev. **D74**, 121503 (2006), gr-qc/0612142.

[46] F. Loffler, L. Rezzolla, and M. Ansorg, Phys.Rev. **D74**, 104018 (2006).

[47] Z. B. Etienne et al., Phys. Rev. **D77**, 084002 (2008), 0712.2460.

[48] Z. B. Etienne, Y. T. Liu, S. L. Shapiro, and T. W. Baumgarte, Phys. Rev. **D79**, 044024 (2009), 0812.2245.

[49] M. D. Duez et al., Phys. Rev. **D78**, 104015 (2008), 0809.0002.

[50] M. D. Duez, F. Foucart, L. E. Kidder, C. D. Ott, and S. A. Teukolsky, Class. Quant. Grav. **27**, 114106 (2010), 0912.3528.

[51] F. Foucart, M. D. Duez, L. E. Kidder, and S. A. Teukolsky (2010), 1007.4203.

[52] S. Chawla, M. Anderson, M. Besselman, L. Lehner, S. L. Liebling, et al., Phys.Rev.Lett. **105**, 111101 (2010), 1006.2839.

[53] M. A. Miller, Phys. Rev. **D71**, 104016 (2005), gr-qc/0502087.

[54] T. Hinderer, B. D. Lackey, R. N. Lang, and J. S. Read, Phys. Rev. **D81**, 123016 (2010), 0911.3535.

[55] T. Damour and A. Nagar, Phys. Rev. **D81**, 084016 (2010), 0911.5041.

[56] L. Baiotti, T. Damour, B. Giacomazzo, A. Nagar, and L. Rezzolla (2010), 1009.0521.

[57] L. Baiotti, T. Damour, B. Giacomazzo, A. Nagar, and L. Rezzolla (2011), 1103.3874.

[58] S. Husa, J. A. González, M. Hannam, B. Brügmann, and U. Sperhake, Class. Quant. Grav. **25**, 105006 (2008), 0706.0740.

[59] M. Hannam, S. Husa, F. Ohme, D. Müller, and B. Brügmann, Phys. Rev. **D82**, 124008 (2010), 1007.4789.

[60] L. Baiotti, B. Giacomazzo, and L. Rezzolla, Class.Quant.Grav. **26**, 114005 (2009), 0901.4955.

[61] D. Pollney et al., Phys. Rev. **D76**, 124002 (2007), 0707.2559.

[62] B. Brügmann et al., Phys. Rev. **D77**, 024027 (2008), gr-qc/0610128.

[63] B. Brügmann, W. Tichy, and N. Jansen, Phys. Rev. Lett. **92**, 211101 (2004), gr-qc/0312112.

[64] B. Brügmann, Int. J. Mod. Phys. **D8**, 85 (1999), gr-qc/9708035.

[65] F. Banyuls, J. A. Font, J. M. A. Ibanez, J. M. A. Marti, and J. A. Miralles, Astrophys. J. **476**, 221 (1997).

[66] K. Taniguchi and E. Gourgoulhon, Phys. Rev. **D66**, 104019 (2002), gr-qc/0207098.

[67] T. Damour, A. Nagar, M. Hannam, S. Husa, and B. Brügmann, Phys. Rev. **D78**, 044039 (2008), 0803.3162.

[68] L. Baiotti, S. Bernuzzi, G. Corvino, R. De Pietri, and A. Nagar, Phys. Rev. **D79**, 024002 (2009), 0808.4002.

[69] C. Reisswig and D. Pollney (2010), 1006.1632.

[70] C. Bona, J. Massó, E. Seidel, and J. Stela, Phys. Rev. Lett. **75**, 600 (1995), gr-qc/9412071.

[71] M. Alcubierre et al., Phys. Rev. **D67**, 084023 (2003), gr-qc/0206072.

[72] J. R. van Meter, J. G. Baker, M. Koppitz, and D.-I. Choi, Phys. Rev. **D73**, 124011 (2006), gr-qc/0605030.

[73] C. Gundlach and J. M. Martin-Garcia, Phys.Rev. **D74**, 024016 (2006), gr-qc/0604035.

[74] S. L. Shapiro and S. A. Teukolsky, *Black holes, white*

dwarfs, and neutron stars: The physics of compact objects (Wiley, New York, USA, 1983).

[75] P. Haensel, A. Y. Potekhin, and D. G. Yakovlev, *Neutron stars 1: Equation of state and structure* (Springer, New York, USA, 2007).

[76] G. Baym, C. Pethick, and P. Sutherland, Astrophys. J. **170**, 299 (1971).

[77] G. Baym, H. A. Bethe, and C. J. Pethick, Nuclear Physics A **175**, 225 (1971).

[78] P. Haensel and B. Pichon, Astron. Astrophys. **283**, 313 (1994), nucl-th/9310003.

[79] W. D. Arnett and R. L. Bowers, Astrophys. J. Suppl. Series **33**, 415 (1977).

[80] N. Stergioulas and J. L. Friedman, Astrophys. J. **444**, 306 (1995), astro-ph/9411032.

[81] J. S. Read, B. D. Lackey, B. J. Owen, and J. L. Friedman, Phys. Rev. **D79**, 124032 (2009), 0812.2163.

[82] J. M. Lattimer and M. Prakash, Phys. Rept. **442**, 109 (2007), astro-ph/0612440.

[83] F. Ozel and D. Psaltis, Phys. Rev. **D80**, 103003 (2009), 0905.1959.

[84] A. W. Steiner, J. M. Lattimer, and E. F. Brown, Astrophys. J. **722**, 33 (2010), 1005.0811.

[85] N. Andersson and K. D. Kokkotas, Mon. Not. Roy. Astron. Soc. **299**, 1059 (1998), gr-qc/9711088.

[86] H. Shen, H. Toki, K. Oyamatsu, and K. Sumiyoshi, Nucl. Phys. **A637**, 435 (1998), nucl-th/9805035.

[87] J. M. Lattimer and F. D. Swesty, Nucl. Phys. **A535**, 331 (1991).

[88] G. Shen, C. J. Horowitz, and S. Teige (2011), 1101.3715.

[89] G. Shen, C. J. Horowitz, and E. O'Connor (2011), 1103.5174.

[90] E. O'Connor and C. D. Ott, Class. Quant. Grav. **27**, 114103 (2010), 0912.2393.

[91] J. A. Font, Living Rev. Rel. **11**, 7 (2007).

[92] J. M. Marti and E. Mueller, Living Rev. Rel. **2**, 3 (1999), astro-ph/9906333.

[93] S. Bernuzzi and D. Hilditch, Phys. Rev. **D81**, 084003 (2010), 0912.2920.

[94] A. Kurganov and E. Tadmor, J. Comp. Phys. **160**, 214 (2000).

[95] L. Del Zanna, N. Bucciantini, and P. Londrillo, Astron. Astrophys. **400**, 397 (2003), astro-ph/0210618.

[96] L. Del Zanna, O. Zanotti, N. Bucciantini, and P. Londrillo (2007), 0704.3206.

[97] H. Nessyahu and E. Tadmor, J. Comp. Phys. **87**, 408463 (1990).

[98] C. Shu and S. Osher, J. Comput. Phys. **77**, 439 (1989).

[99] C. Shu and S. Osher, J. Comput. Phys. **83**, 32 (1989).

[100] A. Harten, P. Lax, and B. van Leer, SIAM Rev. **25**, 35 (1983).

[101] A. Lucas-Serrano, J. A. Font, J. M. Ibanez, and J. M. Marti, Astron. Astrophys. **428**, 703 (2004), astro-ph/0407541.

[102] M. Shibata and J. A. Font, Phys. Rev. **D72**, 047501 (2005), gr-qc/0507099.

[103] E. F. Toro, *Riemann Solvers and Numerical Methods for Fluid Dynamics* (Springer-Verlag, 1999), 2nd ed.

[104] J. A. Font, N. Stergioulas, and K. D. Kokkotas, Mon. Not. Roy. Astron. Soc. **313**, 678 (2000), gr-qc/9908010.

[105] P. Colella and P. R. Woodward, J. Comput. Phys. **54**, 174 (1984).

[106] J. M. Marti and E. Müller, J.Fluid.Mech. **258**, 317 (1994).

[107] A. Mignone, T. Plewa, and G. Bodo (2005), astro-ph/0505200.

[108] X. Liu and S. Osher, J. Comput. Phys. **142**, 304 (1998).

[109] L. Del Zanna and N. Bucciantini, Astron. Astrophys. **390**, 1177 (2002), astro-ph/0205290.

[110] L. Baiotti et al., Phys. Rev. **D71**, 024035 (2005), gr-qc/0403029.

[111] D. Neilsen, E. W. Hirschmann, and R. S. Millward, Class. Quant. Grav. **23**, S505 (2006), gr-qc/0512147.

[112] L. Baiotti, M. Shibata, and T. Yamamoto, Phys. Rev. **D82**, 064015 (2010), 1007.1754.

[113] C. B. Macdonald and S. J. Ruuth, J. Sci. Comput. **35**, 219 (2008), doi:10.1007/s10915-008-9196-6, URL http://people.maths.ox.ac.uk/~macdonald/lscpm.pdf.

[114] G. Jiang, J. Comp. Phys. **126**, 202 (1996).

[115] A. Tchekhovskoy, J. C. McKinney, and R. Narayan, Mon. Not. Roy. Astron. Soc. **379**, 469 (2007), 0704.2608.

[116] G. Corvino, L. Rezzolla, S. Bernuzzi, R. De Pietri, and B. Giacomazzo, Class. Quant. Grav. **27**, 114104 (2010), 1001.5281.

[117] F. D. Swesty, J.Comput.Phys. **127**, 118 (1996), ISSN 0021-9991.

[118] P. Haensel and A. Y. Potekhin, Astron. Astrophys. **428**, 191 (2004), astro-ph/0408324.

[119] T. Nozawa, N. Stergioulas, E. Gourgoulhon, and Y. Eriguchi, Astron. Astrophys. Suppl. Ser. **132**, 431 (1998), gr-qc/9804048.

[120] H. Dimmelmeier, J. A. Font, and E. Müller, Astron. Astrophys. **388**, 917 (2002), astro-ph/0204288.

[121] M. Hannam, S. Husa, D. Pollney, B. Brügmann, and N. O'Murchadha, Phys. Rev. Lett. **99**, 241102 (2007), gr-qc/0606099.

[122] M. D. Duez, Y. T. Liu, S. L. Shapiro, and B. C. Stephens, Phys. Rev. **D72**, 024028 (2005), astro-ph/0503420.

[123] M. Shibata and K. Uryu, Class. Quant. Grav. **24**, S125 (2007), astro-ph/0611522.

[124] J. A. Faber, T. W. Baumgarte, Z. B. Etienne, S. L. Shapiro, and K. Taniguchi, Phys. Rev. **D76**, 104021 (2007), 0708.2436.

[125] P. J. Montero, J. A. Font, and M. Shibata, Phys. Rev. **D78**, 064037 (2008), 0805.3099.

[126] L. Baiotti and L. Rezzolla, Phys. Rev. Lett. **97**, 141101 (2006), gr-qc/0608113.

[127] M. Thierfelder, S. Bernuzzi, D. Hilditch, B. Brugmann, and L. Rezzolla, Phys.Rev. **D83**, 064022 (2011), 1012.3703.

[128] M. Shibata, Phys. Rev. **D67**, 024033 (2003), gr-qc/0301103.

[129] L. Baiotti, I. Hawke, P. J. Montero, and L. Rezzolla, Mem. S.A.It. Suppl. **1**, 210 (2010), 1004.3849.

[130] I. Cordero-Carrion et al., Phys. Rev. **D79**, 024017 (2009), 0809.2325.

[131] L. Baiotti, I. Hawke, L. Rezzolla, and E. Schnetter, Phys. Rev. Lett. **94**, 131101 (2005), gr-qc/0503016.

[132] B. Friedman and V. R. Pandharipande, Nuclear Physics A **361**, 502 (1981).

[133] C. P. Lorenz, D. G. Ravenhall, and C. J. Pethick, Physical Review Letters **70**, 379 (1993).

[134] K. D. Kokkotas and J. Ruoff, Astron. Astrophys. **366**, 565 (2001), gr-qc/0011093.

[135] S. Bernuzzi and A. Nagar, Phys. Rev. **D78**, 024024 (2008), 0803.3804.

[136] J. Martí and E. Müller, J. Comput. Phys. **123**, 1 (1996).

[137] M. Ruiz, D. Hilditch, and S. Bernuzzi, Phys. Rev. **D83**, 024025 (2011), 1010.0523.

[138] L. Baiotti, I. Hawke, and L. Rezzolla, Class. Quant. Grav. **24**, S187 (2007), gr-qc/0701043.

[139] S. Brandt and B. Brügmann, Phys. Rev. Lett. **78**, 3606 (1997), gr-qc/9703066.

[140] J. D. Brown, Phys. Rev. **D77**, 044018 (2008), 0705.1359.

[141] Eric Gourgoulhon, Philippe Grandclment, Jean-Alain Marck, Jrme Novak and Keisuke Taniguchi, *Paris Observatory, Meudon section - LUTH laboratory*, http://www.lorene.obspm.fr/.

[142] E. Gourgoulhon, P. Grandclement, K. Taniguchi, J.-A. Marck, and S. Bonazzola, Phys. Rev. **D63**, 064029 (2001), gr-qc/0007028.

[143] A. Akmal, V. R. Pandharipande, and D. G. Ravenhall, Phys. Rev. **C58**, 1804 (1998), nucl-th/9804027.

[144] M. Bejger et al., Astron. Astrophys. **431**, 297 (2005), astro-ph/0406234.

[145] M. Shibata and K. Taniguchi, Phys. Rev. **D73**, 064027 (2006), astro-ph/0603145.

[146] M. Hannam, S. Husa, U. Sperhake, B. Brügmann, and J. A. González, Phys. Rev. **D77**, 044020 (2008), 0706.1305.

[147] M. Shibata, T. W. Baumgarte, and S. L. Shapiro, Astrophys. J. **542**, 453 (2000), astro-ph/0005378.

[148] L. Baiotti, R. De Pietri, G. M. Manca, and L. Rezzolla, Phys. Rev. **D75**, 044023 (2007), astro-ph/0609473.

[149] O. Zanotti, L. Rezzolla, L. Del Zanna, and C. Palenzuela, Astron. Astrophys. **523**, A8 (2010), 1002.4185.

[150] I. Hawke, F. Loffler, and A. Nerozzi, Phys. Rev. **D71**, 104006 (2005), gr-qc/0501054.

[151] D. Müller and B. Brügmann, Class. Quant. Grav. **27**, 114008 (2010), 0912.3125.

[152] C. O. Lousto, H. Nakano, Y. Zlochower, and M. Campanelli, Phys. Rev. Lett. **104**, 211101 (2010), 1001.2316.

[153] C. O. Lousto, H. Nakano, Y. Zlochower, and M. Campanelli, Phys. Rev. **D82**, 104057 (2010), 1008.4360.

[154] C. O. Lousto and Y. Zlochower, Phys. Rev. Lett. **106**, 041101 (2011), 1009.0292.

[155] E. Schnetter, Class. Quant. Grav. **27**, 167001 (2010), 1003.0859.

[156] D. Müller, J. Grigsby, and B. Brügmann, Phys. Rev. **D82**, 064004 (2010), 1003.4681.

[157] D. Alic, L. Rezzolla, I. Hinder, and P. Mosta, Class. Quant. Grav. **27**, 245023 (2010), 1008.2212.

[158] E. Berti et al., Phys. Rev. **D76**, 064034 (2007), gr-qc/0703053.

[159] J. G. Baker et al., Phys. Rev. **D78**, 044046 (2008), 0805.1428.

[160] S. Bernuzzi, A. Nagar, and A. Zenginoglu, Phys.Rev. **D83**, 064010 (2011), 1012.2456.

[161] G. M. Manca, L. Baiotti, R. De Pietri, and L. Rezzolla, Class.Quant.Grav. **24**, S171 (2007), 0705.1826.

[162] F. Echeverria, Phys.Rev. **D40**, 3194 (1989).

[163] N. Stergioulas, A. Bauswein, K. Zagkouris, and H.-T. Janka (2011), 1105.0368.

[164] D. Pollney, C. Reisswig, E. Schnetter, N. Dorband, and P. Diener, Phys. Rev. **D83**, 044045 (2011), 0910.3803.

[165] J. M. Marti, J. M. Ibanez, and J. A. Miralles, Phys. Rev. **D43**, 3794 (1991).

[166] D. J. Dean, C. Bottcher, M. R. Strayer, J. C. Wells, A. von Keitz, Y. Pürsün, D. Rischke, and J. A. Maruhn, Phys. Rev. E **49**, 1726 (1994).

[167] A. Dolezal and S. S. M. Wong, J. Comput. Phys. **120**, 266 (1995), ISSN 0021-9991.

[168] For this reason the expected end state of the simulation is not exactly model A0 but a model with a smaller mass.

[169] HMNSs are differentially rotating NSs with mass larger than the maximum mass of the corresponding (same EoS) stable uniformly rotating star. Stable configurations of uniformly rotating stars with mass larger than the maximum allowed for the stability in the spherical case do exist, supported by centrifugal forces. They are called supra-massive NSs and rotate at the mass-shedding limit.

[170] The tortoise radius is computed as $r_* = r_{\mathrm{Schw}} + 2M \log(r_{\mathrm{Schw}}/(2M) - 1)$, where r_{Schw} is the Schwarzschild radius corresponding to the isotropic radius r. The retarded time based on this coordinate, $t_{\mathrm{ret}} = t - r_*$, is a useful but approximate quantity which becomes rigorous only at large radii when the spacetime becomes Schwarzschild. The correspondence dynamics-waveform in the simulation is thus biased by this approximation.